Ocean Modelling 86 (2015) 15–35

Contents lists available at ScienceDirect

Ocean Modelling

journal homepage: www.elsevier.com/locate/ocemod

Stochastic simulations of ocean waves: An uncertainty quantification study

B. Yildirim [a,*], George Em Karniadakis [b]

[a] Department of Geophysics, Stanford University, Stanford, CA 94305, USA
[b] Division of Applied Mathematics, Brown University, Providence, RI 02912, USA

ARTICLE INFO

Article history:
Received 20 June 2014
Received in revised form 29 November 2014
Accepted 3 December 2014
Available online 15 December 2014

Keywords:
Ocean wave modeling
Uncertainty quantification
Generalized polynomial chaos
Sparse grid collocation
Sensitivity analysis
Karhunen–Loeve decomposition

ABSTRACT

The primary objective of this study is to introduce a stochastic framework based on generalized polynomial chaos (gPC) for uncertainty quantification in numerical ocean wave simulations. The techniques we present can be easily extended to other numerical ocean simulation applications. We perform stochastic simulations using a relatively new numerical method to simulate the HISWA (Hindcasting Shallow Water Waves) laboratory experiment for directional near-shore wave propagation and induced currents in a shallow-water wave basin. We solve the phased-averaged equation with hybrid discretization based on discontinuous Galerkin projections, spectral elements, and Fourier expansions. We first validate the deterministic solver by comparing our simulation results against the HISWA experimental data as well as against the numerical model SWAN (Simulating Waves Nearshore). We then perform sensitivity analysis to assess the effects of the parametrized source terms, current field, and boundary conditions. We employ an efficient sparse-grid stochastic collocation method that can treat many uncertain parameters simultaneously. We find that the depth-induced wave-breaking coefficient is the most important parameter compared to other tunable parameters in the source terms. The current field is modeled as random process with large variation but it does not seem to have a significant effect. Uncertainty in the source terms does not influence significantly the region before the submerged breaker whereas uncertainty in the incoming boundary conditions does. Considering simultaneously the uncertainties from the source terms and boundary conditions, we obtain numerical error bars that contain almost all experimental data, hence identifying the proper range of parameters in the action balance equation.

1. Introduction

We first present an overview of the action balance equation along with the numerical model, a description of the HISWA experiment, and a review of the stochastic modeling approach we employ. We then present the objectives of this work and the organization of the rest of the paper.

1.1. Phase-averaged equation and source terms

We model ocean waves through the spectral ocean wave equation (Holthuijsen, 2007; Young, 1999) also referred to it as phased-averaged model. We solve for the energy density (or action density) to obtain important statistical wave parameters, such as the significant wave height, mean wave period, etc. The phase-averaged model is well suited for slowly varying wave fields, such as ocean waves in deep water, and it is more appropriate for large spatial domains (Battjes, 1994). In contrast, the model simulating the surface elevation in space and time is called phase-resolving, and is more efficient for waves in a small region of the sea such as a harbor (Battjes, 1994). The spectral ocean representation is essentially a superimposition of many different linear harmonic waves to represent complex ocean surface waves.

Today, most operational ocean codes employ the phase-averaged model. Some of the most well-known codes are SWAN (Simulating Waves Near-Shore) available from http://www.swan.tudelft.nl/, ECWAM (European Center Wave Model) available from http://www.ecmwf.int/, and NOAA's WAVEWATCH available from http://polar.ncep.noaa.gov/waves/. These established operational wave codes employ up to third-order of finite difference discretization in Tolman (1995) for spatial derivatives. To be able to construct arbitrary order of discretization with this new scheme is its biggest advantage over the traditional discretization methods. Although finite difference on structured mesh is an established and efficient method and relatively easy to implement,

* Corresponding author. Tel.: +1 650 723 3120.
E-mail address: yildirim@stanford.edu (B. Yildirim).

http://dx.doi.org/10.1016/j.ocemod.2014.12.001
1463-5003/

it is not well suited for complex geometries, e.g. in coastal applications. Recent effort to use finite difference on unstructured mesh for spectral wave model can be found in the work of Zijlema (2010). On the other hand, the finite element (FE) and finite volume (FV) methods that work on a general grid offer an accurate and efficient algorithm. Recent works have incorporated these methods into the wave models to handle complex coastal boundaries (Hsu et al., 2005; Qi et al., 2009).

1.2. High-order numerical model

Recently we introduced a new numerical method for the spectral ocean wave equations (Yildirim and Karniadakis, 2012), which is distinctively different from previous approaches (Booij et al., 1999; Hsu et al., 2005; Qi et al., 2009; Zijlema, 2010) and employs high-order discretization. Specifically, we compute the spectral space derivatives by Fourier-collocation while we discretize the physical space using a discontinuous Galerkin (DG) method (Yildirim and Karniadakis, 2012; Karniadakis and Sherwin, 1999; Hesthaven and Warburton, 2007; Cockburn et al., 2000). The DG discretization in geophysical space is performed on an unstructured grid to handle the complex boundaries. The overall scheme has exponential convergence rather than algebraic convergence typical of low-order schemes. We have verified the exponential convergence in both the geophysical and spectral spaces in previous work (Yildirim and Karniadakis, 2012). The low-order methods associated with strong numerical dissipation and phase errors smear out the amplitude of solution and shift the position of it. In long time integrations, the accumulated numerical dissipation and phase errors become so large that accurate simulation is not possible. Numerical diffusion test case for first order scheme presented in Booij et al. (1999) shows that first-order scheme is not suitable for the long distance wave propagation. High-order discretization is particularly effective for long-time integration, which is typically required to eliminate the associated dissipation and phase errors in the deep ocean wave simulations.

1.3. HISWA tank experiment

The HISWA experiment (Dingemans, 1987; Dingemans et al., 1986) is a laboratory experiment conducted for random, short-crested waves to validate numerical spectral ocean models (Holthuijsen et al., 1989). This is benchmark experiment that provides measurements for comparisons with simulations and it is one of the most comprehensive works for wave propagation in a laboratory. It includes three different bathymetry shapes as (1) a flat basin, (2) a simple one (fully cylindrical bar), and (3) a complicated one (semi-cylindrical bar with a rounded head), as well as many different operating and boundary conditions. The water level is set to 40 cm from the flat bottom. We chose the complex shape bathymetry (semi-cylindrical with rounded head; see its depth contours in Fig. 1(left)) for this study. The shape of the submerged breakwater can be exactly generated by using the transformations given in Dingemans et al. (1986).

In particular, we consider case me35, where '3' and '5' denote, respectively, bathymetry of semi-cylindrical bar with round over and a specific input in (Dingemans et al., 1986). The input case 5 has specified incoming waves with relatively wide JONSWAP spectrum (Hasselmann et al., 1973) and significant wave height of 10 cm, peak period of 1.25 s, and directional spreading of 25°. The peak enhancement factor of JONSWAP spectrum γ is chosen 3.3 with the spreading widths ($\sigma_A = 0.07, \sigma_B = 0.09$). Case 5 is considered here because this case contains most of the processes that also occur in nature. The current field has been measured at 81 points on a grid of 3 by 3 m at half the water depth. The experiment was done on a relatively large rectangular basin 26 m × 34 m. The wave maker generates waves from left (along $x = 0$ line, see Fig. 1) to the right. This experiment has been used to validate the SWAN model (Ris, 1997).

1.4. Stochastic modeling and uncertainty quantification (UQ)

The spectral wave models contain source terms to represent important wave physics (wave generation, white-capping, depth-induced breaking, and bottom friction) and wave interactions (triads, quadruplets). Among them, we know the exact mathematical expression only for nonlinear wave interactions (quadruplets) (Hasselmann, 1962) but for computational efficiency we have to adopt suitable approximations (Lin and Perrie, 1998; van Vledder et al., 2000; Lavrenov, 2003; van Vledder, 2006; Cavaleri et al., 2007); for the rest of the source terms we employ other empirical models, see Appendix A. In our work, we have adopted a bottom friction parametrization of the source terms from WAMDI Group (1988) using the so-called *third-generation* ocean wave prediction model, source term parametrization of triad interactions from Eldeberky (1996) and of depth-induced breaking from Battjes and Janssen (1978) and Battjes and Stive (1985). Although waves in the HISWA experiment are not generated by wind, we point out that wind input dominates (as a single source of energy into the system) in the modeling of wind-generated waves (Komen et al.,

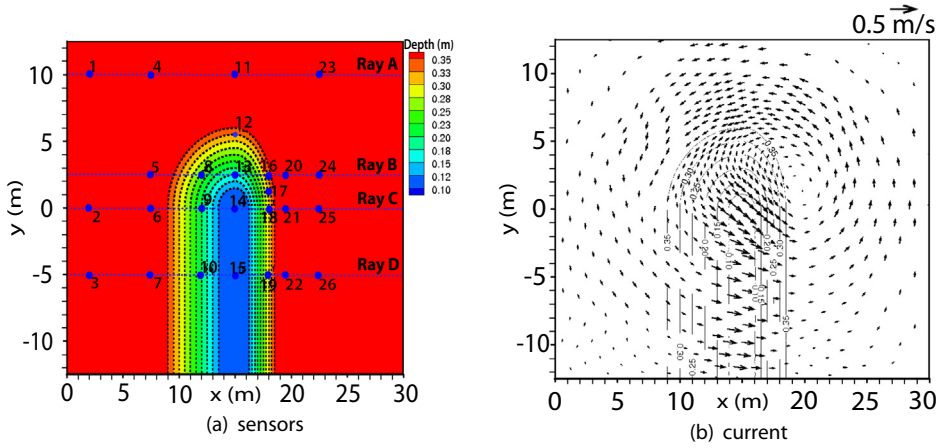

Fig. 1. *HISWA experiment*: sensor locations and bathymetry contours (left) and current vector field (right).

1994; Janssen, 2004; Holthuijsen et al., 1989). The most recent modelings were reviewed by the WISE Group lead by Cavaleri et al. (2007). The parametrization of the source terms is one of the main sources of uncertainty in the spectral ocean wave model. Other sources of uncertainty include bathymetry, current field, and boundary conditions. Data assimilation techniques are usually applied to estimate such uncertain parameters, but this requires specific field measurements, which may not always be available. Here, we will use sensitivity analysis to assess the effect of most of the parameters in the spectral ocean wave model in the context of the HISWA experiment. Specifically, in the source terms we use as uncertain parameters the depth-induced breaking, bottom friction, and triad-wave interaction coefficients. We also model as random processes the current field and the incoming boundary conditions. We will first consider the source terms, current field, and incoming boundary condition randomness individually, and subsequently we will include randomness in the source terms and current field at first, and later in the source terms and boundary conditions, in order to perform uncertainty quantification.

Most previous works involving stochastic modeling have been based on Monte-Carlo methods, see Ponce and Ocampo-Torres (1998), Abdalla and Cavaleri (2002), Bouws and Battjes (1982), Bonekamp et al. (2002) and Roulston et al. (2005) and optimization algorithms in Krasnopolsky et al. (2002), Tolman et al. (2005), Tolman and Krasnopolsky (2006) and Tolman and Grumbine (2013). For example, Abdalla and Cavaleri (2002) investigated the effects of wind gustiness and air density variability on wave growth using Monte Carlo simulation with ECWAM. Bouws and Battjes (1982) applied Monte Carlo sampling for refraction of water waves using initial values of wave frequencies and directions of propagation as random variables. Bonekamp et al. (2002) performed Monte Carlo simulation for the Charnock (1955) parameter using an atmosphere-wave coupled version of ECMWF. Monte Carlo (MC) is straightforward to apply but it is a computationally demanding method since a large number of cases need to be run for achieving a moderate to high accuracy. MC methods typically converge as $1/\sqrt{K}$, where K is the number of realizations (Fishman, 1996). Xiu (2010) shows for the viscous Burger's equation (1D), to get the same accuracy of gPC for the converged solutions (up to three significant digits) obtained by a fourth-order expansion with only five realizations, MC method has to run about 10,000 MC realizations. Plant and Holland (2011) and Plant and Holland (2011) applied the Bayesian network model to handle boundary, bathymetry, and parameter uncertainties. Singular-Vector perturbation methods, also referred as optimal perturbations, using linear tangent propagator to project small perturbations along with trajectory of the nonlinear equations from initial time t_0 to some future time t. They are successfully used in numerical weather prediction (NWP) models for uncertainty prediction (Buizza and Palmer, 1995; Hartmann et al., 1995; Palmer et al., 1997; Gelaro et al., 1997). Perturbation methods have a low computational cost similar to gPC methods. Main disadvantage of perturbation methods (Ehrendorfer and Tribbia, 1997) is that the smallness assumption for introduced perturbations (typically less than 10 percent) around the linearization. The variability of some wave parameters is quite large that perturbation methods may not perform well.

In the current work we will use the generalized polynomial chaos (gPC) framework (Ghanem and Spanos, 1991; Xiu and Karniadakis, 2002), and more specifically the stochastic collocation approach (Xiu and Hesthaven, 2005). The generalized polynomial chaos framework is already popular in many engineering applications for uncertainty quantification but has not been used in quantifying uncertainty in ocean modeling. An exception is some recent work in Thacker et al. (2012) that addresses uncertainties of inflow boundary conditions from the Caribbean Sea in the Gulf's surface elevation field. That work was limited to two dimensions in the parameter space and employed different equations and types of uncertainties from the ones we address herein. In particular, gPC (Xiu and Karniadakis, 2002) is an extension of the classical polynomial chaos (PC) method (Ghanem and Spanos, 1991). The generalization is introduced by using the Askey scheme for hyper-geometric orthogonal polynomials (Xiu and Karniadakis, 2002). In the gPC approach we basically expand the random inputs in terms of orthogonal polynomials chosen according to the density function of the stochastic inputs. To solve the stochastic differential equations efficiently it is better to involve a collocation projection in the parametric space – this is the stochastic collocation method. Hence, applying this projection on each collocation point in random space leads to deterministic governing equations but evaluated at specific (rather than random as in Monte Carlo) points in the parameter space. In summary, in order to perform stochastic simulations using the collocation approach we need two ingredients: (1) a deterministic solver, and (2) the collocation points; the latter are typically roots of the corresponding gPC basis. The important statistical parameters can be readily post-processed from the ensemble. C will present the details of gPC expansion and stochastic collocation methods.

In multi-dimensions, the stochastic collocation method can be constructed by the tensor product of one-dimensional gPC basis using multi-dimensional random variables. However, the number of deterministic runs (N) from the tensor-product construction can be prohibitively expensive ($\mathcal{O}(N^d)$) for large dimensions (d). To this end, the Smolyak grid (see Appendix C) consists of a subset of tensor-product collocation points (Smolyak, 1963 (SparseGridTutorial available at http://page.math.tu-berling.de/garcke/paper/sparseGridTutorial.pdf) to cope with the curse of dimensionality at least for a moderate number of random variables. Specifically, here we employ the sparse grid based on Clenshaw–Curtis quadrature (Clenshaw and Curtis, 1960). The stochastic collocation simulation requires many deterministic runs of the high-order spectral ocean wave code (Yildirim and Karniadakis, 2012) while the number of runs depends on the level and dimensions of the sparse grid. In this work, we used the uncertainty quantification program (PUQ) available at http://memshub.org/site/memosa-docs/puq for generating collocation points for random variables, facilitating job submissions on HPC, and post-processing the ensemble to obtain important statistical parameters such as mean and standard deviation.

1.5. Objectives

In previous work (Yildirim and Karniadakis, 2012) we verified and validated the new high-order method for the action balance equation for: (1) numerical diffusion in geographical space against the finite difference code SWAN (Booij et al., 1999), the finite element code FE-WAVE (Hsu et al., 2005), and the finite volume code FVCOM-SWAVE (Qi et al., 2009); (2) current-induced (four cases: following, opposing, and slanting currents with two different angles) shoaling and refractions in deep water (Phillips, 1966; Longuet-Higgins and Stewart, 1961); (3) depth-induced shoaling and refractions in shallow water (Ris, 1997; Booij et al., 1999); (4) duration-limited growth in deep water (Janssen, 2004); (5) fetch-limited growth in deep water (Breugem and Holthuijsen, 2007; Young and Verhagen, 1996; SWAMP Group, 1985); (6) depth-induced wave breaking, (Battjes and Janssen, 1978), (7) depth-induced wave breaking and triad interactions (Wood et al., 2001).

In the current work, the governing equation includes the directional (due to depth and current variations) and frequency derivatives (due to current field variation) in addition to all three source terms (depth-induced breaking, bottom friction, and triads) for the HISWA simulation. The primary purpose of this work is to perform

a systematic stochastic analysis to assess the adequacy of the parametrization of the source terms, the effect of the current field, and the inlet boundary conditions in the context of the HISWA experiment. This analysis may identify a proper parametric range to be used in other cases as well.

The paper is organized as follows. First, we briefly present the action balance equation (phased-averaged model) in Section 2 and also briefly describe the new high-order scheme in Section 3. Following this section, we present numerical simulation results for various resolutions on a fixed mesh to show the convergence of the scheme. Next in Section 5, we apply stochastic collocation to the HISWA simulation to quantify the uncertainty in such important wave parameters as the significant wave height (H_s), mean wave period (T_{m01}), mean wave direction ($\bar{\theta}$), and energy spectra ($E(f)$). Specifically, we first treat the source parameters (depth-induced breaking, bottom friction, and triads) as random inputs. Subsequently, we add space-dependent random perturbations to the current field and study the combined effects of the random current processes with the random source terms. In the last part of Section 5, we introduce space-dependent random perturbations to the incoming boundary condition and we examine the combined effect of uncertain boundary conditions with uncertain source terms. Finally, we present a brief summary in Section 6. In Appendix A we include some details on the parametrization of the source terms, the details of the numerical discretization that the deterministic code implements is presented in Appendix B, and Appendix C describes the stochastic simulation tools used in this study.

2. Governing equation

The action balance equation (Booij et al., 1999) for ocean waves in the Eulerian framework can be written as

$$\frac{\partial N(\theta,\sigma,x,y,t)}{\partial t}+\frac{\partial c_x N(\theta,\sigma,x,y,t)}{\partial x}+\frac{\partial c_y N(\theta,\sigma,x,y,t)}{\partial y}+\frac{\partial c_\theta N(\theta,\sigma,x,y,t)}{\partial \theta}+\frac{\partial c_\sigma N(\theta,\sigma,x,y,t)}{\partial \sigma}=\frac{S(\theta,\sigma,x,y,t)}{\sigma}, \quad (1)$$

where $N(\theta,\sigma,x,y,t)$ is the *action density* defined as the ratio of energy $E(\theta,\sigma,x,y,t)$ to relative frequency σ ($N=E/\sigma$), c_x and c_y are the propagation velocities of wave energy in physical $(x-y)$ space, and c_θ and c_σ are the propagation velocities in spectral ($\theta\in[-\pi,\pi]$, $\sigma\in[0,\infty]$) space. The explicit expressions of propagation velocities $(c_x,c_y,c_\theta,c_\sigma)$ can be found in Whitham (1974), Holthuijsen (2007) and Yildirim and Karniadakis (2012)). The source term $S(\theta,\sigma,x,y,t)$ accounts for wave generation, dissipation, and wave interaction mechanisms (see Appendix A). The bottom friction process ($S_{\mathrm{b,fr}}$) with bottom friction coefficient $C_{bfr}=0.067$, the depth-induced breaking process S_{br} with $\gamma=0.73$, the scaling coefficient (after Battjes and Janssen, 1978) $\alpha_{BJ}=1.5$, and the triad interactions (S_{nl3}) with the scale factor $\alpha_{EB}=0.5$ are all represented in our model. We also refer the interested readers to WAMDI Group (1988), Komen et al. (1984), Young and Verhagen (1996), Holthuijsen (2007) and Yildirim and Karniadakis (2012) for an in-depth discussion of modeling the source terms.

3. Numerical discretization

We present a concise description of the numerical discretization of phased-averaged ocean wave equation in Appendix B, which we summarize in this section. We use the discontinuous Galerkin (DG) (Hesthaven and Warburton, 2007; Hesthaven et al., 2007; Karniadakis and Sherwin, 1999) method for the geographical space. The spatial discretization is defined on an arbitrary triangle domain to support the unstructured grids, which are most suitable grids for the wave problems on the complex bathymetry and coastal boundaries. The details can be followed on Appendix B.4.

The directional domain extends from $-\pi$ to π. We use *Fourier-collocation* to discretize the directional derivative in Eq. (1). The solutions in many applications may have a very narrow directional spreading; an example is $\cos^m(\theta)$ directional spreading. We see that most of the energy contained in only a very narrow region for higher values of m. The Fourier-collocation employs equi-spaced distribution in the directional domain. We have to employ very high resolution to capture the very narrow region and, depending on the solution steepness, the number of collocation points can be so large that we cannot afford to run such simulations. Alternatively, we define a mapping to cluster the Fourier-collocation points around a specified region (local refinement). We have found that this mapping can save us up to eight times in the number of collocation points in the directional domain. In case that they are many wave fields in the domain or directional peaks keep moving, then the discretization needs a fully adapted directional discretization. The current code is only supporting the static grid that can cluster the grid points around a single specific point. Dynamic grid and multi-points support will be implemented in the future.

The frequency domain ranges from 0 to ∞. We usually truncate the semi-infinite domain into a finite domain as $[f_{min},f_{max}]$. The numerical boundary condition in this domain is non-reflecting. The straightforward Fourier-collocation method cannot be applied for non-periodic boundary conditions. However, we can still use a *Fourier-collocation with an Absorbing Boundary Layer (ABL)* for the wave problem of which the energy spectra asymptotically goes to zero toward the tails. Fourier-collocation has been shown to have advantages over the more traditional Chebyshev method (Boyd, 1988) in the truncated domain. We have used the Absorbing Boundary Layer (ABL) approach (If et al., 1987) to enforce *periodicity* at the frequency domain ends. To this end, we added a modified term to the main Eq. (1) to solve the problem in an extended domain $[f_{min}-\triangle_L,f_{max}+\triangle_R]$ that we obtained by adding the absorbing layers $\triangle_L$ and $\triangle_R$, respectively, on the left (f_{min}) and the right (f_{max}). The modified term takes zero values inside the domain and hence we solve the Eq. (1) backwards. The Absorbing Boundary Layer function defined in Yildirim and Karniadakis (2012) controls the modified term in the absorbing boundary layers and introduces heavy dissipation to smear out the solution. The current code is able to generate logarithmic distribution for the frequency direction when the domain is free of a current field. To define logarithmic distribution in frequency direction for a problem that has a current field with non-zero gradient, we should propose a similar mapping as it is done for the directional grid. Similar to a tan mapping B.5 used for the directional grid, a log mapping (Boyd, 2001) can create a logarithmic distribution around the specific frequency in the frequency grid. Since the current code can not generate a logarithmic distribution in the frequency direction for the certain cases, the application of the code is limited for general applications. The disadvantage of using uniform grid that deploys the finer frequency grid to resolve the high-gradients (in frequency direction) is that it will over-resolve the smooth regions, wasting computer resources and increasing computation time. To be more efficient, this new scheme should define a mapping in frequency grid that generates a logarithmic distribution of points.

We compute the spectral derivatives for each grid point (θ_i,σ_i) in the spectral space. Each grid point now has an equation in geographical space. We then applied *discontinuous Galerkin (DG)* discretization (Hesthaven and Warburton, 2007; Hesthaven et al., 2007; Karniadakis and Sherwin, 1999) to this equation. We refer the interested readers to Yildirim and Karniadakis (2012) for details of spatial discretization of the action balance equation.

With regards to temporal discretization, we employed second- and third-order (Gottlieb and Shu, 1998), as well as the

fourth-order explicit (5-stages) (Spiteri and Steven, 2001) *Strong Stability Preserving Runge–Kutta* (SSP-RK) schemes.

4. Validation studies

4.1. Numerical simulation ($S = S_{\mathrm{b,fr}} + S_{\mathrm{br}} + S_{\mathrm{nl3}}$)

The computational domain in geophysical space (see Fig. 2(a)) $[(0, 30)\ \mathrm{m} \times (-45, 45)\ \mathrm{m}]$ is discretized into 48 triangular elements in conjunction with a spectral collocation grid whose frequency axis ranges from 0.4 Hz to 3.0 Hz with resolution 0.04 Hz (equi-spaced grid along the frequency direction), and the directional domain lying in $[-60^\circ, 60^\circ]$ with resolution about 4° around the center and about 20° around the tails. The directional collocation points are generated by local refinement using the arctan mapping as given in Yildirim and Karniadakis (2012); which clusters the collocation points around the center. The directional domain size $[-60^\circ, 60^\circ]$ is sufficient to resolve most of the energy for the me35 case that has directional spreading width given as 25°. We used a left absorbing boundary layer width as 0.2 Hz and a right one as 1.0 Hz, which effectively extended the frequency domain from $[0.4, 3.0]$ Hz to $[0.2, 4.0]$ Hz.

We applied the incoming energy spectrum on the left boundary using the JONSWAP spectrum (see Eq. (7)) with directional spreading model $\cos^m(\theta - \theta_0)$ (Holthuijsen, 2007), where θ_0 is the reference incoming wave direction and we set $m = 4$ based on the given directional width of 25°. The JONSWAP spectrum (Holthuijsen, 2007; Hasselmann et al., 1973) of peak frequency f_p used here of 0.8 Hz, scale parameter $\alpha = 0.0154$, peak-width parameters $\sigma_a = 0.07$ and $\sigma_b = 0.09$ are chosen to represent the significant height of 10 cm for the incoming wave boundary condition. The centered reference direction (θ_0) in the directional distribution is interpolated from measurement locations 1–2–3 (along the y-axis, see Fig. 1) and projected on the left boundary. We assume that in the computational boundary outside the ray A and ray D lines (see Fig. 1) the reference direction (θ_0) is zero. The lateral boundaries are naturally reflective, but in our implementation we do not take this into account, which is not significant in this case (me35) since in the experiment wave generators send waves perpendicular (not obliquely) to the left boundary; hence, we specified zero energy along these boundaries. This is inherently a dissipative process and pollutes the numerical solution inside the domain. We extended the lateral boundaries y_{min} to -45 and y_{max} to 45 for minimizing the numerical boundary pollution in the region of interest (see dashed region in Fig. 2(a)). The experiment was designed to minimize any reflection on the right end and hence we set non-reflecting boundary conditions at this end. We set the initial condition to zero energy in the domain for all runs.

The interpolated current field from the experiment was provided by N. Booij from Digital Hydraulics Holland (private communication). This current field is interpolated to the collocation points (see Fig. 2(a) right)) in the simulation. The current field of the computational grid outside the experimental area is assumed to be zero; the current vector field is shown in Fig. 1 (right).

Bottom friction and depth-induced wave breaking are the important dissipation processes with nonlinear wave-wave interactions (only triads). The source parameters are chosen based on the suggestion of Ris (1997) whose results we used here for the SWAN comparison. Our numerical simulation results verified that the important wave parameters are insensitive to quadruplet interactions (S_{nl4}), which is also observed in the work of Ris (1997). Quadruplet interactions are turned off for the HISWA simulation in the entire paper.

The computation is carried out by marching in time (our implementation currently supports only unsteady computation) to reach a steady state solution. To this end, we march the unsteady solution with the time step 0.025 s up to the final time 35 s. The Runge–Kutta second-order time integration scheme is employed for all cases in the entire paper. In space, first-, third-, and fifth-order of the Jacobi polynomials are expanded over the triangular elements in the computation of this section.

The measurement locations of 26 stations are given in Fig. 1(left). We have measurements for the significant wave height H_s and mean wave period T_{m01} for all 26 locations, but for the mean wave direction $\bar{\theta}$ we have only seven locations (1, 2, 3, 17, 24, 25, 26). The comparison is made on horizontal line Rays C and B rather than all measurement locations (Rays A, B, C, D) to simplify the presentation. Extensive results on the Rays A–D can be found in

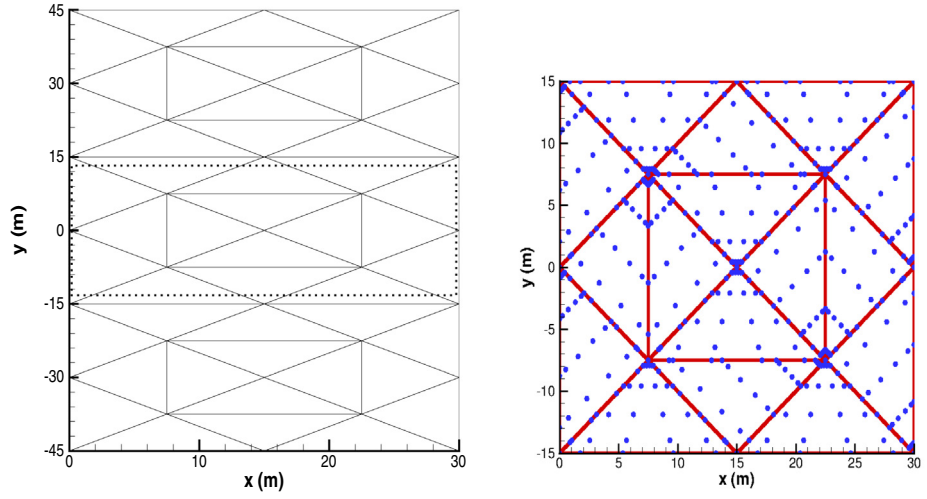

(a) computational mesh (b) zoomed mesh with collocation points

Fig. 2. Computational mesh (48 triangular elements) used for the HISWA simulation. The dashed region (on left) is the experimental region. The mesh (right) is a zoom at the dashed region, and the collocation points on this mesh are represented by blue circles. (For interpretation of the references to colour in this figure legend, the reader is referred to the web version of this article.)

Yildirim (2012). The four rays cover 24 stations and exclude only two stations 12 and 17. The energy spectra are compared for eight locations (5, 3, 13, 15, 16, 19, 24, 26) in this study.

We used the same directional and frequency resolutions while employing three different Jacobi polynomial orders expanded over the triangles. The plots of integrated parameters (H_s, T_{m01} and $\bar{\theta}$) on ray C and energy spectra $E(f)$ of station 24 are presented in Fig. 3. They demonstrate significant improvement from the first-order to the third-order polynomials. The high-order polynomial results ($p = 3, 5$) in Fig. 3 have clearly improved the integrated parameters (H_s, T_{m01} and $\bar{\theta}$) on the ray C measurement locations and energy spectra on station 24. For further comparisons, specifically on results of the integrated parameters on ray A, B, and C locations and energy spectra of seven locations, we refer the interested readers to Yildirim (2012).

The results given in Fig. 3 agree well with the experiment for the significant wave height and mean wave period for the third- and fifth-orders of Jacobi polynomials. The reference SWAN simulation is taken from Ris (1997). The high-order method predicts these two statistical parameters better than SWAN, specifically on Rays B, C, and D (see Yildirim, 2012). However, neither code predicts the mean wave direction accurately on the stations behind the bar, i.e. in stations 24, 25, 26.

The data used to compare here are taken from an older version of the SWAN code (Ris, 1997) because of their availability. We note however that the SWAN code has now enhanced capability, e.g. in solving the ocean wave equation more accurately than before. Fig. 4 adds the data from the most recent (2014) SWAN structured and unstructured codes for the comparison. The new run of SWAN for the HISWA experiment case simulate the energy spectra around main and secondary peaks as accurate as DG code and much better than its older version.

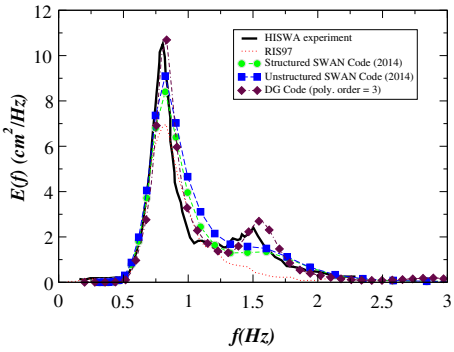

Fig. 4. Energy spectra for the station 24 are presented from HISWA experiment, RIS97 from Ris (1997) (obtained by the earlier version of SWAN code a more than a decade ago), a recent data (2014) from Structured and Unstructured SWAN codes, and DG code ($p = 3$).

5. Uncertainty quantification

Possible sources of uncertainty include modeling errors for the complex and unresolved physics, initial and boundary conditions, geometry and physical properties of the medium. In this study, we will focus on uncertain inputs related to the parametrization of the source terms in the action balance equation, the form of the current field, and the incoming boundary conditions.

In the action balance equation, important wave physics (generation, dissipation, and nonlinear wave interactions) is represented parametrically through the source terms, see Appendix A. The numerical ocean wave community has been actively doing research to improve this representation (WAMDI Group, 1988;

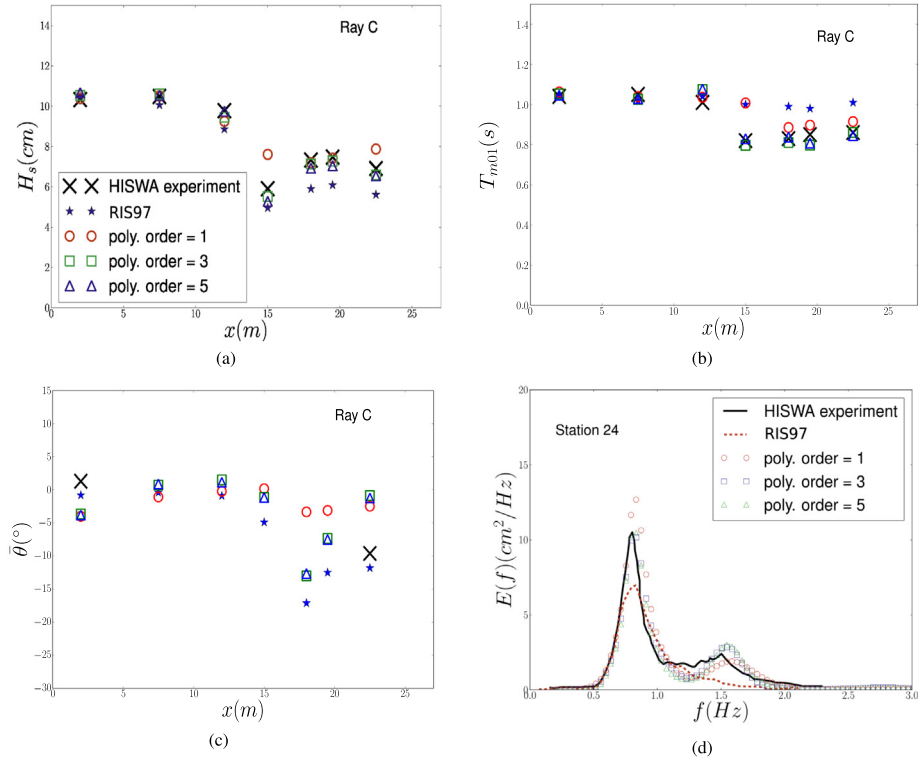

Fig. 3. *Verification of accuracy*: comparison of simulation results (three different polynomial orders ($p = 1, 3, 5$)) for (a) significant wave height (**Hs**), (b) mean wave period (T_{m01}), (c) mean wave direction ($\bar{\theta}$) on ray C, and (d) energy spectra at station 24 against experimental and Ris, 1997 results.

Cavaleri et al., 2007), and improvements in the source terms are reflected in the so-called first-, second-, and third-generation ocean wave models; among them, the third-generation is still the most common model. For the various contributions to the source terms, we have an exact mathematical expression for only the quadruplet wave-wave interactions (Hasselmann, 1962, 1963a,b). Hence, they can be solved exactly as done by Hasselmann and Hasselmann (1985), Snyder et al. (1993), Lin and Perrie (1998) and Benoit (2005) but this leads to excessive computational cost. The rest of the important contributions, including dissipation (white-capping, depth-induced breaking, and bottom friction) and triads have no explicit mathematical expressions and they are modeled empirically in WAMDI Group (1988) through effective parameters. Specifically, we will treat the parameters γ and α_{BJ} in the depth-induced wave breaking source term, the bottom friction coefficient C_{bfr} in the bottom friction term, and the triad coefficient α_{EB} in the triad interaction term as *random* variables.

All runs of our deterministic solver employed third-order Jacobi polynomials on the triangular spectral elements (see mesh in Fig. 2(a)). The time integration scheme, boundary condition, and spectral space size and resolution are all kept the same as in the previous section.

5.1. Sensitivity analysis of source term parameters

The elementary effect method (Morris, 1991) provides a measure of sensitivity from a small number of model evaluations.

Let us consider a function $\mathcal{F}$ that has k independent input parameters such that

$$\mathcal{F} = f(X_1, X_2, \ldots, X_k),$$

where $\mathcal{X} = (X_1, X_2, \ldots, X_k)$ varies in a k-dimensional cube with p level, which selects sampling locations on each dimension. The elementary effect is defined as:

$$d(X_i) = \frac{\mathcal{F}(X_1, X_2, \ldots, X_{i-1}, X_i + \triangle, \ldots, X_k) - \mathcal{F}(X_1, X_2, \ldots, X_k)}{\triangle}, \quad (2)$$

where $\triangle$ is a value chosen equal to $p/(2(p-1))$ for even p. In this method we choose randomly r sample points among p levels ($r < p$). The number of r samples can be considerably smaller than p, and hence the method needs $k \times r$ output evaluations to compute the sensitivity. The random r sample points can be taken from the Smolyak grid (Smolyak, 1963). The elementary effect method uses two measures for mean (μ) and standard deviation (σ) of r elementary effects of each input. The mean (μ) measures the relative influence factor of each input. The mean of r sampling elementary effects is defined (for input X_i) as

$$\mu_i = \frac{1}{r}\sum_{j=1}^{r} d\left(X_i^{(j)}\right). \quad (3)$$

The standard deviation σ assesses nonlinear effects of the input parameters (X_k) (Saltelli et al., 2008). The software PUQ that we use has the capability of post-processing output functions to compute the mean and standard deviations of r sampled elementary effects for the input parameters.

We present the mean values of the input elementary effects for the significant wave height and mean wave period on ray C, and mean wave direction on ray B, C in Fig. 5. The values of the elementary effects signify the degree of importance of each input sensitivity for a specific output. As seen in Fig. 5, the elementary effect values are very low for the three outputs at the front stations. This clearly shows that the numerical solution is not sensitive to the parametrization of the source terms there.

The elementary effect values of the significant wave height H_s in Fig. 5(a) shows that the most important parameter at all locations is γ, i.e. the parameter of depth-induced breaking. The importance ranking among other remaining inputs $C_{bfr}, \alpha_{BJ}, \alpha_{EB}$ depends on the location. The triad coefficient α_{EB} becomes the dominant parameter if we look at the elementary effect values of mean wave period T_{m01} in Fig. 5(b). The depth-induced parameter γ follows the triad coefficient in importance. Hence, it follows that variations in the bottom friction coefficient C_{bfr} and the other depth-induced parameter α_{BJ} affect the mean wave period output equally. The depth-induced coefficient γ is the dominant parameter again for the sensitivity of the mean wave direction output $\bar{\theta}$ as seen in Fig. 5(c) and (d). The remaining parameters C_{bfr}, α_{EB}, and α_{BJ} have about the same order of influence on the mean wave direction.

The main conclusion from the sensitivity analysis performed here is that the elementary effects of each input for the three outputs $(H_s, T_{m01}, \bar{\theta})$ are not uniform in physical space and, therefore, we shall not exclude any of the parameters to reduce the dimensionality of parametric space in this study. We refer the interested reader to Yildirim (2012) for further discussion of results on several other locations.

5.2. Uncertainty in source terms

The parameters in the source terms associated with depth-induced wave breaking, bottom friction, and triads are all non-zero in the code for the HISWA simulation. The depth-induced breaking term has two parameters treated as random variables: the scaling factor $\alpha_{BJ} \in [1.0, 2.0]$ with mean value of 1.5 and the wave breaking coefficient $\gamma \in [0.6, 1.0]$ with mean value of 0.8. The bottom friction coefficient $C_{bfr} \in [0.038, 0.096]$ with mean value of 0.067 is the only random variable in the bottom friction term. The value of 0.038 is recommended for swell conditions by the JONSWAP experiment (Hasselmann et al., 1973) and 0.067 by Bouws and Komen (1983) for fully developed wave conditions in the shallow-water. It is also worth to note that, based on more recent observations, a recent work of Zijlema et al. (2012) shows that the lower value for swell should be preferred for both applications. The tuning parameter of the triad source term $\alpha_{EB} \in [0.0, 1.0]$ with the mean value 0.5 is the final random variable in the source terms.

Here we will assume that the uncertainty is based on a uniform distribution of parameter values on a chosen range (see the above for the ranges). The range of the parameters here are chosen from the values found in the literature. Although the ranges can be more freely chosen, the cost of choosing an unwise short-range that under represents the true parametric range or a large-range that wastes the computational resources since more collocation points (each point in the random space requires a full deterministic simulation) will be needed to get a specified accuracy. For this reason, the uncertainty estimates are still inherently subjective. To examine convergence in parametric space, the mean (μ) and standard deviation (σ) of the solution are evaluated by using the second-, third,- and fourth-order gPC expansion. The four random variables using the Smolyak sparse grid (of level 2, 3, and 4) require 41, 137, and 401 deterministic runs, respectively, for the second-, third-, and fourth-order gPC expansions see Yildirim (2012). The mean values of the three parameters converge even for first-order gPC expansions. The third- and fourth-order expansions do not improve the statistical quantities (the mean and the standard deviation) in the significant wave height. However, the third-order improves the standard deviation in the mean wave period and the mean wave direction. The fourth-order expansion changes slightly the statistical quantities of all three wave parameters. This confirms the convergence of the expansion. Another observation from the standard deviation calculations of all three outputs is that the highest uncertainty is associated with the region behind the bar. The standard deviation values start rising at $x > 12$ m, see Fig. 1.

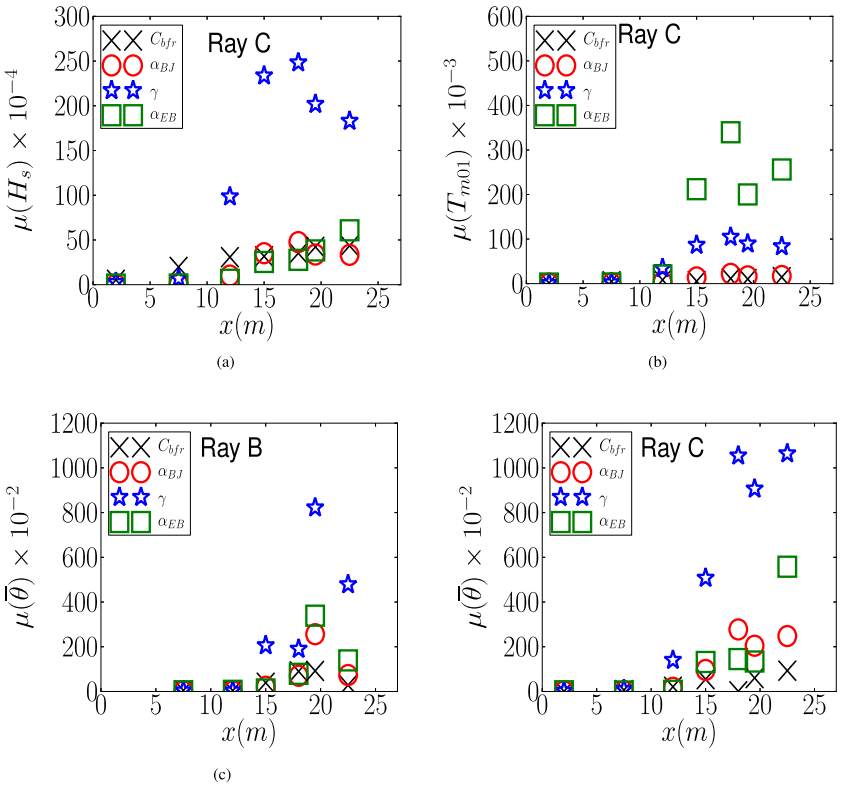

Fig. 5. *Effects of uncertainty in the source terms*: elementary effect values for (a) significant height (H_s), (b) mean wave period (T_{m01}), and (c, d) mean wave direction ($\bar{\theta}$) for four parameters of the source terms ($C_{bfr}, \alpha_{BJ}, \gamma, \alpha_{EB}$).

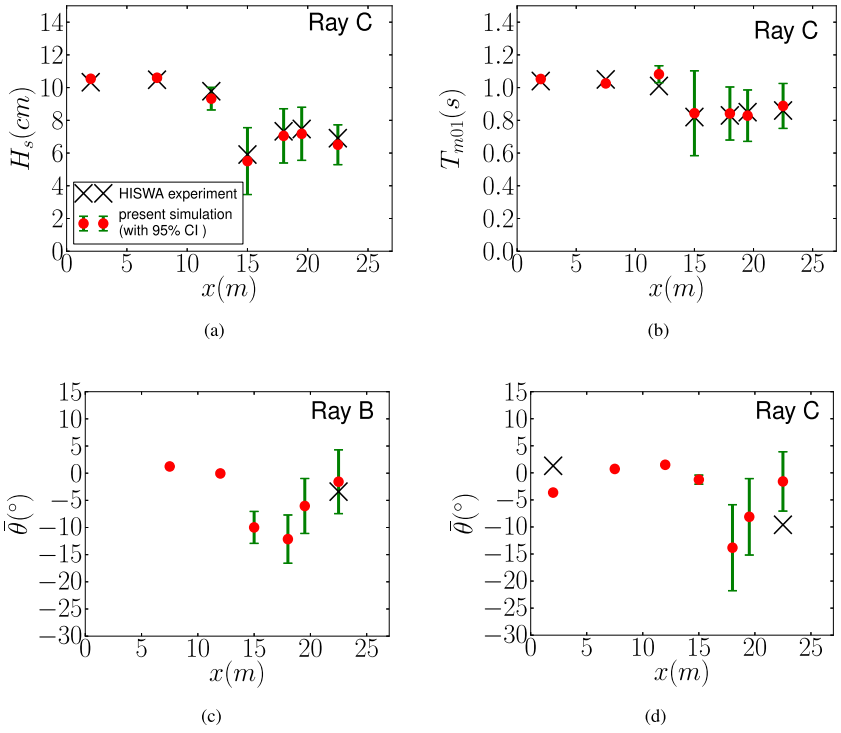

Fig. 6. *Uncertainty in source terms*: Comparison of simulation results for (a) significant wave height H_s, (b) mean wave period T_{m01}, and (c, d) mean wave direction $\bar{\theta}$ (confidence interval within 95% ($\mu \pm 2\sigma$)) against experimental data. We use fourth-order expansion for the sparse grid in the source parameters ($C_{bfr}, \alpha_{BJ}, \gamma, \alpha_{BJ}$).

We present the error bar plots with a confidence interval 95% ($\mu \pm 2\sigma$) around the mean value for stations on rays C and B in Fig. 6. These confidence intervals do not cover the experimental results for the stations on ray A (not presented here). As mentioned before, the standard deviations have low values along ray A. The real issue is that the numerical solution does not match well with that of the experiment due to the fact that we have current field data available for only the physical region but not for the

larger-size computational domain. As mentioned earlier, we extended our lateral boundaries from $y \pm 13$ m to $y \pm 45$ m. The current field is assumed to be zero in this extended region ($-45\text{ m} \leqslant y < -13\text{ m}; 45\text{ m} \geqslant y > 13\text{ m}$). This discrepancy might be the reason for the numerical solution not matching well the measurements along the stations of ray A. The error bars on ray C for significant wave height and mean wave period are given in Fig. 6. They confirm that the confidence interval of 95% covers well the experiment results. Furthermore, we observed that the confidence intervals vary greatly at the region $x \geqslant 15$ behind the submerged breaker. The scarcity of measurement locations (only 7 out of 26) for the mean wave direction makes this judgment harder as to whether or not the confidence intervals (see bottom plots in Fig. 6) cover the experimental measurements. The confidence interval only covers the measurement location on ray B (see ray B subplot in Fig. 6). We see again that the area behind the breaker is the most uncertain region for the mean wave direction. The stations on rays B and C have the largest standard deviation values of the mean wave direction in this region due to the relatively complex bathymetry and the strong current gradient along the B and C. We note that the mean wave direction is treated here as a line moment ($\int \theta D(\theta) d\theta$) rather than as a circular moment ($\int \mathrm{Sin}(2\theta) D(\theta) d\theta$). For small deviation this is not a problem, but for large directional errors this can be a problem (Kuik et al., 1988).

We also present the error bar plots within 95% confidence intervals for the energy spectra of the selected stations on rays B and D in Fig. 7. The numerical simulation and experimental results are compared for the energy spectra of stations on ray B (5, 13, 16, 24) and ray D (3, 15, 19, 26). The left-column and right-column subplots are arranged such that the left plots are for the stations on ray B and the right plots are for the stations on ray D in Fig. 7. The mean value of the energy spectra of stations (red dots) match the experimental spectra better on ray B than the stations on Ray D for the primary peaks. The secondary peaks arise in the numerical simulation but are not as pronounced as in the measurements. The numerical simulation overestimates the primary frequency for station 13 but underestimates the peak frequency at station 16. Additionally, the numerical solution overestimates the

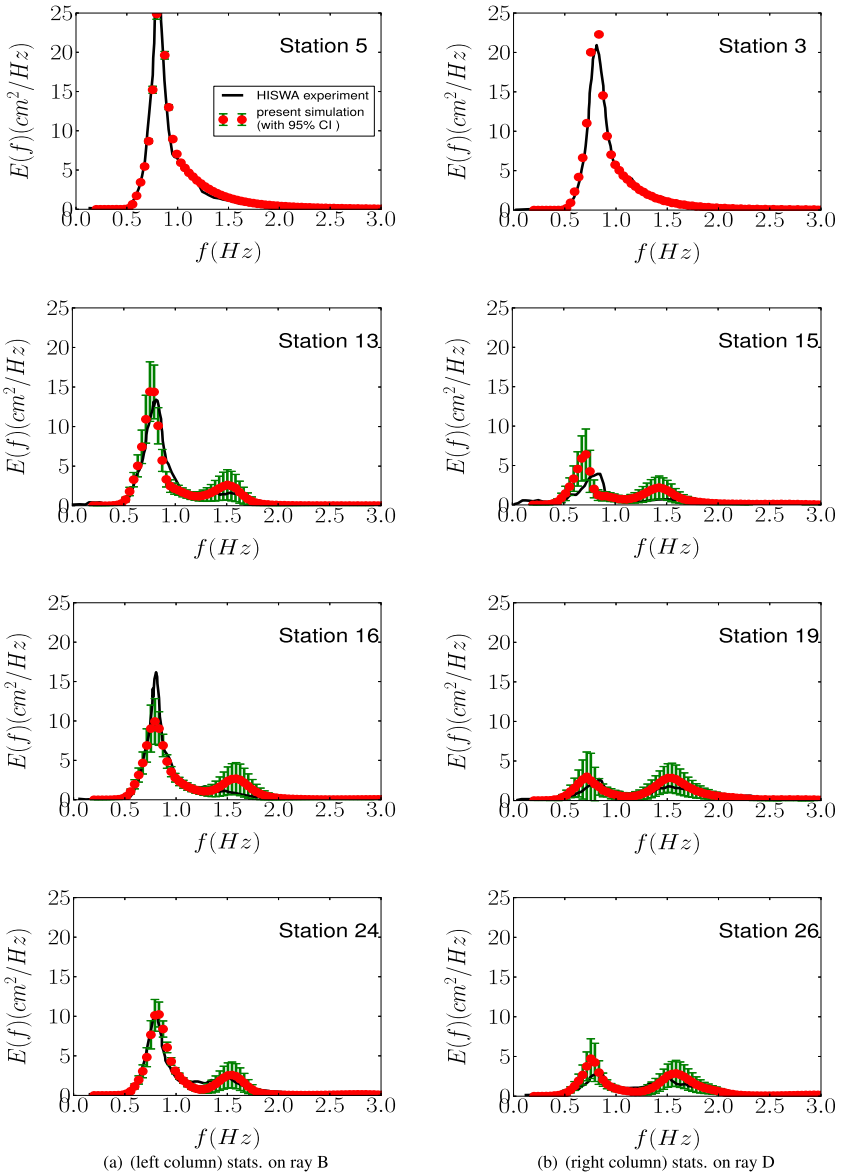

(a) (left column) stats. on ray B (b) (right column) stats. on ray D

Fig. 7. *Uncertainty in the source terms*: Comparison of simulation results (confidence interval within 95% ($\mu \pm 2\sigma$)) against experimental data for the energy spectra. We use fourth-order expansion for the sparse grid in the source parameters ($C_{bfr}, \alpha_{BJ}, \gamma, \alpha_{BJ}$).

secondary peaks for these two stations. The error bars (left-columns) of energy spectra in Fig. 7 show that the confidence intervals capture the measured spectra. Although using a wide range of proper coefficients, the mismatching solutions with the experimental data indicate the inadequacy of the chosen parametrization itself. We point out that the proposed method here only covers the uncertainty introduced through the parameters in a specific model and not any model uncertainty.

As for the stations on ray D, the numerical simulation predicts that the first peaks would be slightly off along the frequency axis for the stations (15, 19) (see right-column plots in Fig. 7). The standard deviation values are relatively large around the secondary peaks for these stations. The confidence intervals seem to cover well the experimental results as seen in the right-column plots in Fig. 7.

5.3. Uncertainty in current field

Next, we consider the two-dimensional current field $\vec{u} = (u_x, u_y)$ as stochastic input in this section, and we employ the Karhunen–Loeve (K–L) decomposition (Loeve, 1977) with a Gaussian correlation function to represent it. The corresponding random process, a function of space, is obtained by adding perturbations via the K–L expansion terms to the experimental realization $\bar{u}(x,y)$, i.e.,

$$u(x,y,\omega) = \bar{u}(x,y) + \delta\sum_{i=1}^{\infty}\sqrt{\lambda_i}\psi_i(x,y)\xi_i(\omega), \tag{4}$$

where $u(x,y,\omega)$ denotes the random processes, $\bar{u}(x,y)$ is the current mean, $\{\xi_i(\omega)\}$ is a set of uncorrelated random variables with zero mean and unit variance and δ is a scalar to control the magnitude of the perturbation. Also, $\{\psi_i(x)\}$ and $\{\lambda_i\}$ are the eigenfunctions and eigenvalues of the covariance kernel $R_{uu}(x_1,x_2)$, that is

$$\int R_{uu}(x_1,x_2)\psi_i(x_2)dx_2 = \lambda_i\psi_i(x_1). \tag{5}$$

We use here the Gaussian correlation function:

$$R_{uu}(x_1,x_2) = \exp\left[-3\frac{(x_1-x_2)^2}{l_c^2}\right], \tag{6}$$

where l_c denotes the correlation length. This length l_c determines the dimension of random space. The random perturbation in Eq. (4) is in practice truncated to P finite dimension. The desired number of finite dimensions M can be chosen by a specified percentage of the perturbation energy $\left(\sum_{i=0}^{P}\lambda_i\Big/\sum_{i=0}^{M}\lambda_i \times 100\right)$. We use here three different correlation lengths relative to domain size: 30 m, 25 m, and 20 m. The resultant number of dimensions of the random space to capture 90% of the energy ($|u\cdot u|$) for the three correlation lengths can be seen in Table 1. The current field vector components u_x and u_y are treated as two separate independent random processes; this doubles the size of the random space dimension given in Table 1. The number of runs using the Smolyak grid (level 2, 3, and 4) are presented in Table 2 for the three different correlation lengths and three different levels.

Table 1
Required number of random dimensions for correlation lengths 30 m, 25 m, and 20 m.

Corr. len. (l_c)	30	25	15
Num. of dimension	4	5	7

Table 2
Required number of runs using the Smolyak grids (level 2, 3, and 4) for the random process current field. Runs 8801 and 30801 were not executed but given here for completeness.

Corr. len. (l_c)	Level 2	Level 3	Level 4
$l_c = 30$ (ndim = 4×2)	145	849	3937
$l_c = 25$ (ndim = 5×2)	221	1581	8801
$l_c = 25$ (ndim = 7×2)	421	4117	30801

The scaling factor δ in the K–L expansion (4) is chosen such that we have perturbation magnitude of 25% with respect to the measured current $\bar{u}(x,y)$. To this end, we took the δ values as 0.0225 for the velocity x-component (u_x) and 0.0175 for the velocity y-component (u_y). The three different correlation lengths are run for the levels 2 and 3 in this section (we do not present these results here). We observed that the mean and the standard deviation values along the stations have quite close values for level 2 and level 3; we chose level 3 in the Smolyak grid for all the runs in this section. We have used a relatively large correlation length in order to keep the random space dimensions sufficiently low so that we perform these simulations within a reasonable time. We first study the influence of the correlation length on the standard deviation of the three wave parameters. The values of standard deviation of significant wave (see Yildirim, 2012), mean wave period, and mean wave direction do not change much for the three correlation lengths (l_c = 30 m,25 m,20 m). The values of the normalized standard deviation (divided by the mean) for the significant wave height and the mean wave period are mostly below 2%. This indicates that introducing a perturbation of magnitude 25% in the current leads to very small uncertainty for these two quantities. The small variations in wave parameters due to somewhat large perturbations in current velocity should be expected since the present current field is the result of gradient in radiation stresses, leading to weak currents.

All the error bar plots have confidence intervals within 95% ($\mu \pm 2\sigma$). The significant wave height results (see Yildirim, 2012) show that uncertainty is very small for the stations on rays B, C, and D. The stations on ray A show larger uncertainty, which may be due to boundary conditions. This issue will be investigated in the following sections. As mentioned earlier, the physical boundaries have been extended along the y-axis, and we assumed the current field to be zero in this extended region. We introduced randomness only in the physical region in the stochastic simulation. Therefore, this ad hoc assumption might cause a relatively larger uncertainty on the stations of ray A.

The random current process has produced very small error bars (see Yildirim, 2012) on all the stations for the mean wave period. Ris (1997) performed similar HISWA simulation with the SWAN code but with the current set to zero and demonstrated that the effects of current on the significant wave height and mean wave period are much less pronounced than expected. We also obtained this result in our stochastic simulations; perturbations of the current field with magnitude 25% changed only slightly the wave parameters (H_s, T_{m01}). On the other hand, we have seen a larger variation in the mean wave direction for almost all stations on rays A–D. This is also in agreement with the results of Ris (1997), who stated the importance of the current field in order to obtain the correct mean wave direction. In particular, Ris (1997) turned off the current field in the numerical simulation and observed that the results of mean wave direction deviated greatly from the experimental values. Extensive results from the current perturbation are presented in Yildirim (2012); they demonstrate that the current has also a negligible effects on the energy spectra for this specific simulation.

5.4. Uncertainty in boundary conditions

The SWAN simulation prescribes the incoming wave boundary conditions based on the HISWA experimental values at locations 1, 2, and 3. The observed wave conditions at the front stations

are not uniform while the mean wave directions for stations 1, 2, and 3 are -5.6°, 1.3°, and -3.6°, respectively. Similarly, the significant wave heights observed on stations 1, 2, and 3 are 11.06 cm, 10.33 cm, and 10.04 cm. We have neglected those variations on the boundary so far and imposed the JONSWAP spectrum on the left boundary condition with the peak frequency ($f_{p0} = 0.8$ Hz) and the incoming wave direction ($\theta_0 = -4.0^\circ$); the JONSWAP spectrum is defined as

$$E_{JONSWAP}(\theta,f) = \begin{cases} A_1 \cos^m(\theta-\theta_0)\alpha_{PM} g^2 (2\pi)^{-4} f^{-5} \exp\left[-\frac{5}{4}\left(\frac{f}{f_{PM}}\right)^{-4}\right] \gamma^{\exp\left[-\frac{1}{2}\left(\frac{f/f_{p0}-1}{\mu}\right)^2\right]}, & |\theta-\theta_0| \leqslant 90^\circ, \\ 0, & |\theta-\theta_0| > 90^\circ, \end{cases} \tag{7}$$

where γ is a peak-enhancement factor and μ is a controlling parameter of spectrum width, and A_1 is defined as $\Gamma(m/2+1)/[\Gamma(m+1)/2)\sqrt{\pi}]$ (m controls the width parameter in a directional spectrum, see Holthuijsen (2007) for the details). The relevant parameter values for the JONSWAP spectrum used here are given in Section 4.1.

We consider non-uniform boundary conditions at the left boundary modeled as random processes. To this end, we will take the peak frequency f_0 and incoming wave direction θ_0 as the random processes and incorporate them into the left boundary. We employ the K–L decomposition of a Gaussian correlation function to represent the random processes of the peak frequency $f_{p0}(x,y)$ and of incoming mean wave direction $\theta_0(x_L,y)$. The random process of incoming peak frequency can be written as

$$f_{p0}(x_L,y,\omega) = \bar{f}_{p0}(x_L,y) + \delta\sum_{i=1}^{\infty}\sqrt{\lambda_i}\psi_i(x_L,y)\xi_i(\omega), \tag{8}$$

where $f_{p0}(x_L,y,\omega)$ denotes random processes of incoming peak frequency and $\bar{f}_{p0}(x_L,y)$ is the incoming peak frequency mean. The incoming peak frequency mean is taken as 0.8 Hz.

Similarly, we can write the K–L expansion for the incoming wave direction as

$$\theta_0(x_L,y,\omega) = \bar{\theta}_0(x_L,y) + \delta\sum_{i=1}^{\infty}\sqrt{\lambda_i}\psi_i(x_L,y)\xi_i(\omega), \tag{9}$$

where $\theta_0(x_L,y,\omega)$ is random process of incoming wave direction and $\bar{\theta}_0(x_L,y)$ is incoming wave direction mean. The incoming wave direction mean is assumed to be -4.0°. Here $\{\xi(\omega)\}$ is a set of uncorrelated random variables, and $\{\psi_i(x)\}$ and $\{\lambda_i\}$ are the eigenfunctions and eigenvalues of the covariance kernel $R_{bb}(x_1,x_2)$, that is

$$\int R_{bb}(x_1,x_2)\psi_i(x_2)dx_2 = \lambda_i\psi_i(x_1). \tag{10}$$

We use here the Gaussian correlation function:

$$R_{bb}(x_1,x_2) = \exp\left[-3\frac{(x_1-x_2)^2}{l_c^2}\right], \tag{11}$$

where l_c denotes the correlation length. Note that R_{bb} is defined only for the left boundary ($[x_L = 0, y = (-45,45)]$). The random processes are introduced to the computational grid nodes at the left boundary. The boundary condition in our high-order ocean wave code is linearly interpolated to the Gauss–Lobatto quadrature points of boundary face from these grid nodes. The correlation length l_c determines the dimension of random space, here we set it to 15 m, i.e., equal to triangle edge length on the boundary side. The dimension of the above covariance kernel in this case is the number of left boundary grid nodes, which is seven. The resulting dimension of the random space capturing 100% of the energy (see Section 5.3) for this correlation length is seven for each random process. The total dimension of the random space will be 14 accounting for both processes.

The perturbation scale is δ in the K–L expansions in Eqs. (8) and (9) based on the variation of mean wave direction and significant wave heights of experiment at the sites 1, 2, and 3. The mean wave direction is chosen as -4°, which is equal to the average observational values between site 1 (-5.6°) and 3 (-3.6°); site 2 has an observational value of 1.3°. The perturbation scale for the mean wave direction is chosen as 5.0 so that the perturbation lies between -8° and 2°. As for peak frequency random process, the perturbation scale is taken as 0.08 to have a variation corresponding to perturbation of 10%; this is based on the variation of observed significant wave heights at sites 1, 2, and 3, which are respectively 11.06 cm, 10.33 cm, and 10.04 cm.

The mean and the standard deviations are well converged for level 2 and level 3 gPC expansions. We chose level 3 for the Smolyak grid for this section. The dimension of random space will be 14 for level 3 expansion, which requires 4117 deterministic runs.

We present the error bar plots (only on ray B and C) for the three statistical wave parameters ($H_s, T_{m01}, \bar{\theta}$) in Fig. 8. All the error bar plots shown here have confidence intervals within 95% ($\mu \pm 2\sigma$). The first important observation is that we have larger uncertainties at the locations before the breaker than we observed due to the uncertainty in the source term parametrization for the significant wave height parameter (see plots (a) in Figs. 8 and 6). The significant wave height error bars are smaller at the locations stationed behind the submerged breaker ($x > 15$ m). Since depth-breaking is the dominant process in the HISWA experiment, it is not surprising to see that variations in the boundary have been damped across the submerged bar. For ray A, which is not affected so much from the changing bathymetry, there is large variation everywhere (results not shown here, see Yildirim (2012)). The random boundary conditions strongly affect the mean wave period results as seen in Fig. 8(b). We have treated the incoming mean wave direction also as a random process. Accordingly, we see large variation about the mean around the ray B and C stations in Fig. 8(c) and (d); the variations are increased after the submerged breaker. We observe large variations around the front stations, which were not observed due to uncertainties in source terms and current field.

5.5. Uncertainty of source and boundary condition

Next we study the *combined effect* of randomness in the source terms and boundary conditions. The four random variables of the source terms ($\alpha_{BJ}, \gamma, C_{br}$, and α_{EB}) follow a uniform probability distribution within the range specified in Section 5.2. The dimension of random space is the sum of 14 random variables from the K–L expansions of the random processes of the incoming peak and wave direction (see Eqs. (8) and (9)) and the four random variables in the source parametrization. The total number of deterministic runs for level 3 and the eighteen variables is 8509. Our results are presented in Figs. 9–11. The experimental values of significant wave height are all contained within 95% confidence interval along the rays A–D as seen in Fig. 9. The confidence intervals are significantly modified for the stations along ray A and the front stations

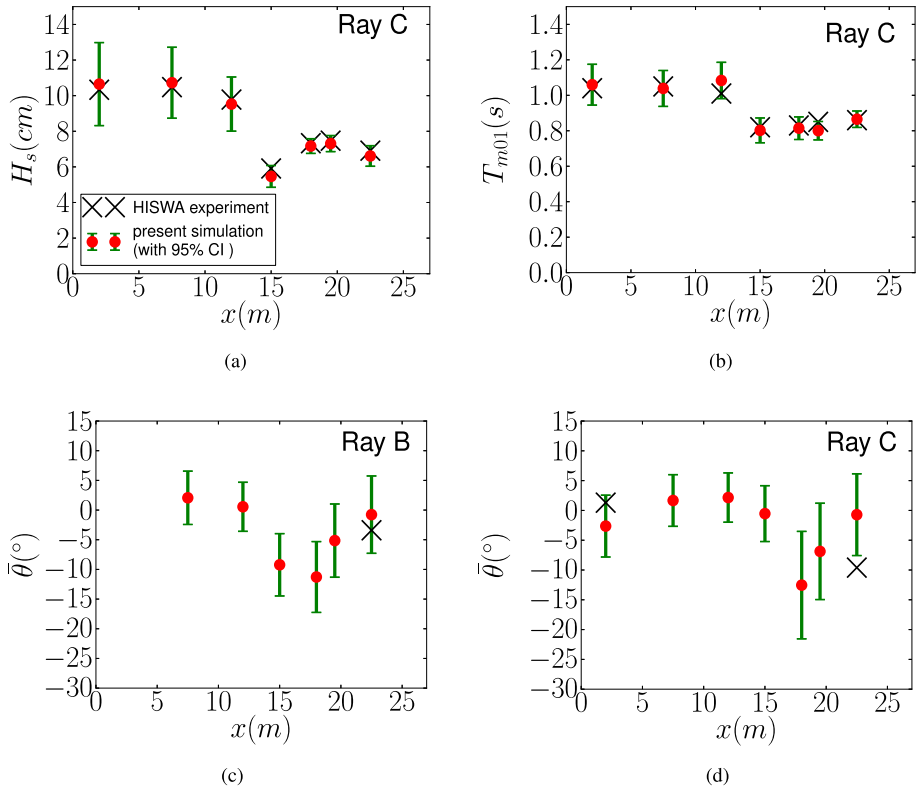

Fig. 8. *Uncertainty in boundary conditions*: Comparison of simulation results for (a) significant wave height H_s, (b) mean wave period T_{m01}, and (c, d) mean wave direction $\bar{\theta}$ (within 95% Confidence Interval ($\mu \pm 2\sigma$)) against experimental data. We use third-order expansion for the sparse grid in the random process of boundary parameters ($\bar{\theta}_0(x,y)$ and $f_p(x,y)$) with correlation length = 15 m.

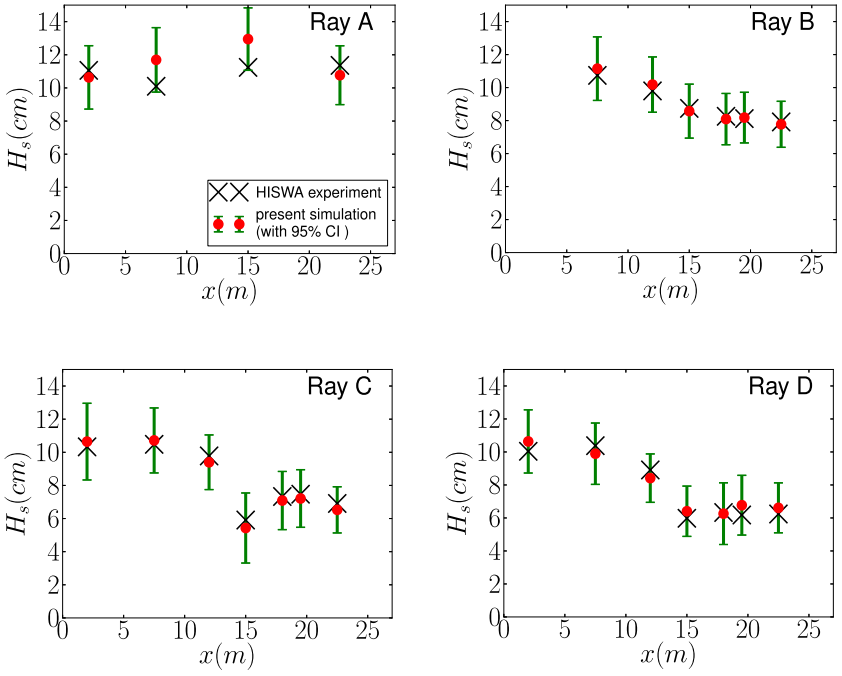

Fig. 9. *Uncertainty in source term and boundary conditions*: Comparison of simulation results for significant wave height H_s (within 95% Confidence Interval ($\mu \pm 2\sigma$)) against experimental data. We use third-order expansion for the sparse grid in the random process of boundary parameters ($\bar{\theta}_0(x,y)$ and $f_p(x,y)$) with correlation length = 15 m and in the source parameters ($C_{bfr}, \alpha_{BJ}, \gamma, \alpha_{EB}$).

along rays B–D due to the boundary random processes. However, the stations beyond ($x > 15$ m) on rays B–D have almost the same level of confidence intervals as in the source uncertainty only case. The measured values of mean wave period are all contained within 95 percent confidence interval along the rays A–D. The confidence intervals of ray A and front stations of rays B–C are strongly influenced by the boundary random processes relative to those of source uncertainty (see plot (b) in Figs. 6 and 10 for ray C).

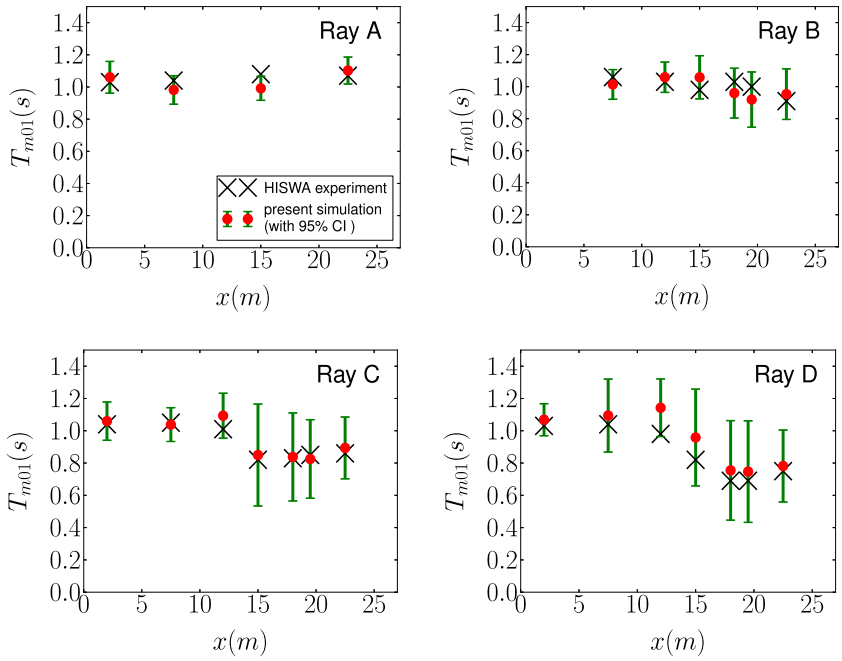

Fig. 10. *Uncertainty in source term and boundary conditions*: Comparison of simulation results for mean wave period T_{m01} (within 95% Confidence Interval ($\mu \pm 2\sigma$)) against experimental data. We use third-order expansion for the sparse grid in the random process of boundary parameters ($\bar{\theta}_0(x,y)$ and $f_p(x,y)$) with correlation length = 15 m and in the source parameters ($C_{bfr}, \alpha_{BJ}, \gamma, \alpha_{EB}$).

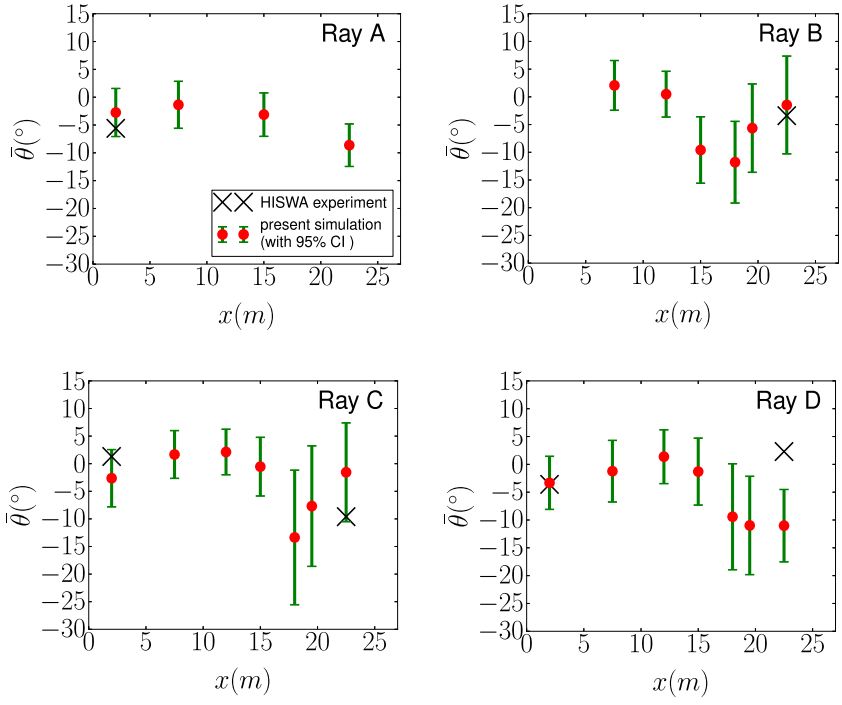

Fig. 11. *Uncertainty in source term and boundary conditions*: Comparison of simulation results for mean wave direction $\bar{\theta}$ (within 95% Confidence Interval ($\mu \pm 2\sigma$)) against experimental data. We use third-order expansion for the sparse grid in the random process of boundary parameters ($\bar{\theta}_0(x,y)$ and $f_p(x,y)$) with correlation length = 15 m and in the source parameters ($C_{bfr}, \alpha_{BJ}, \gamma, \alpha_{EB}$).

However, here these influences in Fig. 10 are extended to the stations downstream of the submerged breaker for the mean wave period, which is not the case in the significant wave height results. Here, the incoming mean wave direction is treated as random process at the boundary. The mean wave direction results along ray A–D show now larger confidence intervals than those due to source uncertainty (see Fig. 6); the results are presented in Fig. 11. The incorporation of boundary random processes into the left boundary along with source uncertainty enlarges the confidence intervals at all stations along rays A–D.

The energy spectra for ray B and D stations are given in Fig. 12. The confidence intervals within 95 percent are amplified at the front stations. The confidence intervals contain almost all measurement values from the experiment.

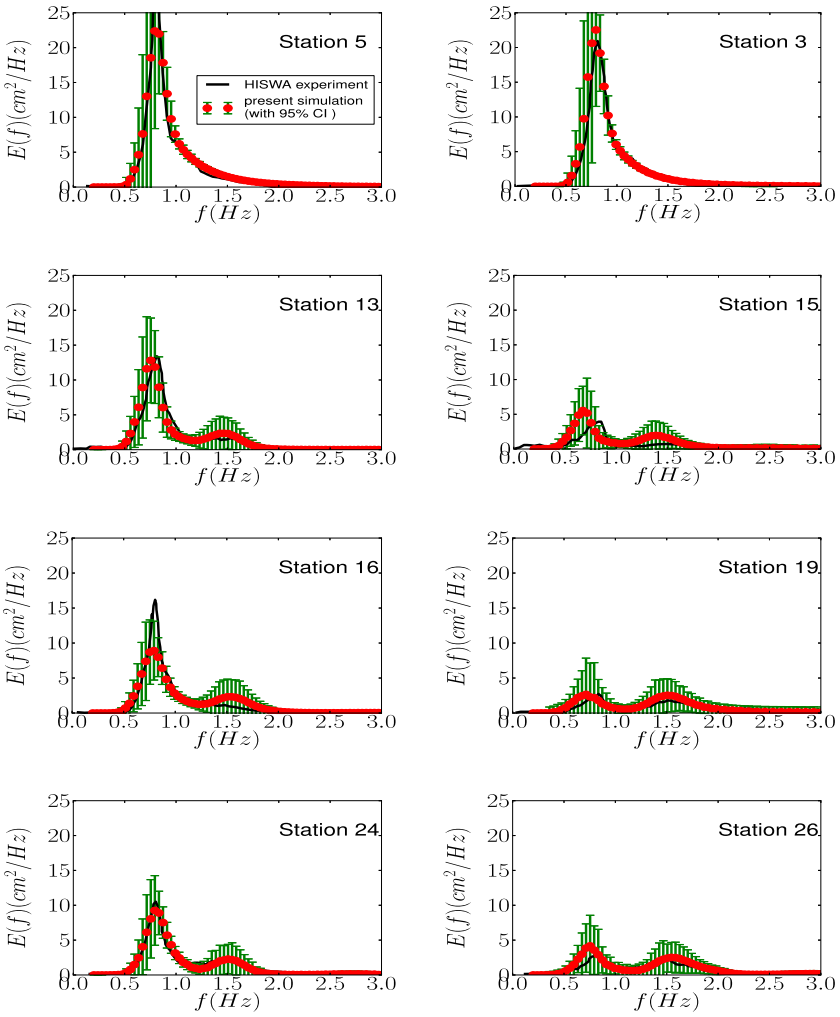

(a) (left column) stats. on ray B (b) (right column) stats. on ray D

Fig. 12. *Uncertainty in source term and boundary conditions*: Comparison of simulation results for energy spectra (confidence interval within 95% ($\mu \pm 2\sigma$)) and experimental data. We use third-order expansion for the sparse grid in the source parameters ($C_{bfr}, \alpha_{BJ}, \gamma, \alpha_{BJ}$) and in the K–L expansion coefficients of incoming peak frequency ($f_p(x,y)$) and ($\overline{\theta}_0(x,y)$) mean wave direction as random process.

6. Summary and conclusions

We have validated a new high-order scheme proposed in Yildirim and Karniadakis (2012) using the HISWA experiment. We used a coarse triangular mesh in which different Jacobi polynomial orders ($p = 1, 3, 5$) are expanded over the triangular elements. The first-order of Jacobi polynomial expansion was too low to capture the important wave parameters of the HISWA experiment. The third- and fifth-orders of the Jacobi polynomials significantly improved the result on the same coarse mesh.

We have also performed sensitivity analysis of the source term parameters used in this simulation. We looked at three different outputs: (1) significant wave height, (2) mean wave period, and (3) mean wave direction. The depth-induced breaking parameters γ and α_{BJ}, bottom friction coefficient C_{bfr}, and triad parameter α_{EB} all seem important either for some region of the domain or for one of the three wave outputs. The sensitivity results suggested to keep the parametrization of the three source terms as random inputs for uncertainty quantification.

We conducted stochastic simulations to quantify the uncertainty in the HISWA simulation. We considered randomness in the source term parametrization, current field, and boundary condition in this study. The source term uncertainty and random current field were individually treated first and then combined. We used the second-, third-, and fourth-order expansion of gPC for stochastic simulation with random inputs for the source parametrization. We compared the mean and standard deviations of the three wave parameters (see Yildirim, 2012 for detailed results). The results suggested that the third-order expansion was converged. We have only shown plots of confidence intervals within 95% in Fig. 6 for ray B, C stations; the complete set of results can be found in Yildirim (2012). We see that the confidence intervals within 95% captured well the experimental results for the significant wave height and mean wave period (see plots (a) and (b) in Fig. 6). As for the mean wave direction (see plots (c) and (d) in Fig. 6), the stations after the wave breaker have shown larger confidence interval variations. But the confidence intervals within 95% did not contain the experimental results at ray C or ray D (not shown here). The rightmost measurement on ray C (see plot (d) in Fig. 6) can be covered by the confidence intervals 99% ($\mu \pm 3\sigma$). We remark that the source term parametrization has small influence on the three wave parameters on the stations of ray A or on the stations before the wave breaker ($x < 12$).

The confidence intervals within 95% of the energy spectra are shown in Fig. 7. The intervals are significantly larger around the primary and secondary peaks for all stations. The energy spectra from the experiment are also well contained by the confidence intervals from the stochastic simulation for the source random input.

The current field has a direct influence on depth-induced and current-induced wave refraction and shoaling. We introduced a random current field by using the Karhunen–Loeve expansion of the exponential Gaussian correlation function. The correlation length determines the dimension of random space. We have tested three different correlation lengths: 30 m, 25 m, and 20 m; these results are not presented here but they can be found in Yildirim (2012). We briefly mention that the standard deviation of the three important wave parameters (H_s, T_{m01}, $\bar{\theta}$) did not make a significant difference between level 3 and level 4 expansion from the Smolyak grid. We chose the correlation length as 25 m and used the level 3 from the Smolyak grid for stochastic simulation of the random current input. Perturbations with magnitude of about 25% were introduced to x and y velocity components of the experimental current field. Although it is a relatively large perturbation of the current field, the confidence intervals (see the results in Yildirim (2012)) did not induce any noticeable differences in the significant wave height or the mean wave period.

The error bars of energy spectra were slightly changed around the primary peaks at the stations (see detailed results in Yildirim (2012)) where strong current gradients were present. For this perturbation level, the uncertainty of source term parametrization still has a much larger effect than the random current field input on the wave parameters and energy spectra.

The incoming wave direction and peak frequency at the left boundary were treated as random processes. The error bar plots are presented for the three important integrated parameters in Fig. 8. An important observation is that we see larger variation around ray A stations and the front stations of ray B–D for the integrated parameters (only ray C and B results are presented here). The variations are relatively smaller toward the downstream stations for the significant wave height and mean wave periods. However, we see larger error bars on the downstream stations for the mean wave direction.

We also performed stochastic simulations by considering combined sources of uncertainty. First we combined two random sources (source and current) to perform a stochastic simulation. The resulted error plots (not shown here) reflect the same level of uncertainty as the one resulted from parametrization of the source only. This, in turn, implies the dominance of the uncertainty from the source terms. Adding to the uncertainty from boundary conditions to both fields (source and current) will increase the dimension of the random space on a level that we cannot afford the computational cost. Since the uncertainty of the current field barely changes the overall outcome, the relevant statistics for the integrated wave parameters can be obtained by dropping the uncertainty of the current field and combining two random sources from the source term parametrization and boundary condition. Hence, such stochastic simulation will yield the combined uncertainty from all the inputs (source terms, current field, and boundary condition). The error bars with confidence intervals within 95% are shown in Figs. 9–11. The confidence intervals covered well the observational values from the experiment except the value on the experimental station of ray D for the mean wave direction. Fig. 12 shows that the confidence intervals contained well the experimental measurements for the energy spectra for the probe stations. Wherever a large variation of the confidence intervals occurs (such as around the first and secondary peaks) it signifies the sensitivity of a solution to the input parameters.

Acknowledgments

This work was supported by the MIT Sea Grant Program and by DOE. The authors would like to thank Dr. N. Booij (Digital Hydraulics Holland) for providing the experimental data to us and to the anonymous reviewers for providing the SWAN simulation data and their valuable comments and suggestions to improve the quality of the paper.

Appendix A. Source terms

A.1. Triad wave-wave interactions (S_{nl3})

The Lumped Triad Approximation (LTA) by Eldeberky (1996) is the simplest expression for triad wave interactions. The approximation is

$$S_{nl3}(\theta,\sigma) = S^{-}_{nl3}(\theta,\sigma) + S^{+}_{nl3}(\theta,\sigma), \tag{A.1}$$

and the positive term contribution is computed as

$$S^{+}_{nl3} = \max\left[0, \alpha_{EB} 2\pi c c_g J^2 |\sin\beta| \left\{E^2(\theta,\sigma/2) - 2E(\theta,\sigma/2)E(\theta,\sigma)\right\}\right], \tag{A.2}$$

where α_{EB} is a control parameter. The negative contribution of source terms can be defined in terms of the positive one as

$$S^{-}_{nl3} = -2S^{+}_{nl3}(\theta, 2\sigma). \tag{A.3}$$

The bi-phase parameter β is approximated by using the Ursell number Ur:

$$\beta = -\frac{\pi}{2} + \frac{\pi}{2}\tanh\left(\frac{0.2}{Ur}\right), \tag{A.4}$$

and

$$Ur = \frac{g}{8\sqrt{2}\pi^2}\frac{H_s T^2_{m01}}{d^2}. \tag{A.5}$$

The coefficient J (Madsen and Sørenson, 1993) can now be defined as

$$J = \frac{k^2_{\sigma/2}\left(gd + 2c^2_{\sigma/2}\right)}{k_\sigma d\left(gd + \frac{2}{15}gd^3k^2_\sigma - \frac{2}{5}\sigma^2 d^2\right)}. \tag{A.6}$$

A.2. Depth-induced wave breaking (S_{br})

The mean rate of energy dissipation due to depth-induced breaking is:

$$D_{tot} = -\frac{1}{4}\alpha_{BJ} Q_b \left(\frac{\tilde{\sigma}}{2\pi}\right) H^2_{max}, \tag{A.7}$$

where the value of α_{BJ} is of the order of one. The fraction of breaking waves is represented by Q_b, which is derived by assuming cumulative probability distributions of all waves (Battjes and Janssen, 1978; Battjes and Stive, 1985) from the following relation:

$$\frac{1 - Q_b}{\log Q_b} = -8\frac{H_{rms}}{H^2_{max}}, \tag{A.8}$$

where H_{rms} is the root-mean-square of wave height and H_{max} is the maximum wave height for a given depth. The maximum wave height is defined as $H_{max} = \gamma d$. The breaker parameter γ is chosen as an default average value of 0.73 from the work of Battjes and Stive (1985).

The depth-induced wave breaking source term (Eldeberky, 1996) can be modeled as

$$S_{br}(\theta,\sigma) = \frac{D_{tot}}{E_{tot}} E(\theta,\sigma). \tag{A.9}$$

Note that S_{br} will have a negative sign due to D_{tot}.

A.3. Bottom friction (S_{bfr})

Bottom friction is modeled from WAMDI Group (1988) based on further simplification of the bottom friction model of the JONSWAP experiment (Hasselmann et al., 1973) as

$$S_{bfr}(\theta,\sigma) = -C_{bfr}\frac{\sigma^2}{g^2\sinh^2(kd)}E(\theta,\sigma), \tag{A.10}$$

where C_{bfr} is the tunable bottom friction coefficient. The modeling of the bottom friction source term assumes that the tangential stress on the bottom can be modeled by a quadratic friction law (Hasselmann and Collins, 1968), which can be interpreted in terms of the bottom friction source term, leading to the above formulation (Hasselmann et al., 1973). In the JONSWAP experiment (Hasselmann et al., 1973) 10 swell cases were tested and showing that the bottom friction coefficient changes from 0.03 to 0.16, with a mean value of $0.038\ m^2\ s^{-3}$. The bottom friction coefficient $C_{bfr} = 0.067\ m^2\ s^{-3}$ has been used by Bouws and Komen (1983) for fully developed waves in shallow water. The coefficient C_{bfr} is not constant but depends on the bottom amplitude Reynolds number and the bed roughness. We refer the interested readers to Young's book (Young, 1999) for further discussion and references.

Appendix B. Numerical discretization

We presented a detailed description of numerical discretization of phased-averaged ocean wave equation in our previous work (Yildirim and Karniadakis, 2012; Yildirim, 2012), which will be summarized in this section. Let us now define the following fluxes with the transformation of the frequency coordinate $\sigma \to \zeta = \pi\left[\frac{2(\sigma-\sigma_{\min})}{\sigma_{\max}-\sigma_{\min}} - 1\right]$:

$$E = c_x N(\zeta,\theta,x,y,t), \quad F = c_y N(\zeta,\theta,x,y,t), \quad G = c_\theta N(\zeta,\theta,x,y,t),$$
$$H = c_\zeta N(\zeta,\theta,x,y,t).$$

Using the above definitions, the action balance equation in flux form is written as

$$\frac{\partial N}{\partial t} + \frac{\partial E}{\partial x} + \frac{\partial F}{\partial y} + \frac{\partial G}{\partial \theta} + J_{\zeta\sigma}\frac{\partial H}{\partial \zeta} = \frac{S}{\sigma}, \tag{B.1}$$

where $J_{\zeta\sigma} = 2\pi/(\sigma_{\max} - \sigma_{\min})$.

B.1. Fourier-collocation methods for the spectral derivatives

We use Fourier-collocation in a directional domain extending from $-\pi$ to π due to periodicity. The frequency direction (σ) is usually a truncated domain, which is non-periodic. This, in turn, makes a standard Fourier-collocation along the frequency direction applying impossible. The numerical solution passing the boundaries should not be reflected by the truncated ends to a computational domain. A modification to apply the standard Fourier-collocation for the derivative term along the frequency axis, using absorbing boundary layer approach (If et al., 1987), was proposed in our previous work (Yildirim and Karniadakis, 2012), and it will be described in Appendix B.3. Let us discretize the wave direction θ and the transformed frequency direction (ζ) as

$$\theta_k = -\pi + \frac{2\pi}{N}k \quad \forall k \in [0,1,\ldots,N-1],$$
$$\zeta_l = -\pi + \frac{2\pi}{N}l \quad \forall l \in [0,1,\ldots,N-1],$$

and then using Lagrangian interpolation (Gottlieb and Orszag, 1977; Hesthaven et al., 2007), we can compute

$$\left.\frac{\partial G}{\partial \theta}\right|_{\theta=\theta_k} = \sum_{j=0}^{N-1} D_{kj} G(\zeta,\theta_j,x,y,t), \tag{B.2}$$

where D_{kj} is the differentiation matrix for Fourier-collocation. Similarly, we obtain

$$\left.\frac{\partial H}{\partial \zeta}\right|_{\zeta=\zeta_l} = \sum_{j=0}^{N-1} D_{lj} H(\zeta_j,\theta,x,y,t). \tag{B.3}$$

The differentiation matrix (Hesthaven et al., 2007) for an even number of collocation points (Lagrangian polynomial if $q = 0$) reads in a dummy coordinate z (either θ or ζ to obtain the above flux derivatives)

$$D_{ij}^q = \frac{2}{N}\sum_{n=0}^{N/2}\frac{1}{c_n}\begin{cases}(in)^q\cos[n(z_i - z_j)], & q \text{ even}\\ i(in)^q\sin[n(z_i - z_j)], & q \text{ odd}\end{cases} \tag{B.4}$$

where $c_0 = c_{N/2} = 2$ and $c_n = 1$, otherwise. For an odd number of collocation points, the same differentiation matrix can be used by setting $c_n = 1$ for all values of n.

B.2. Mapping in the spectral direction

The standard Fourier-collocation employs equi-spaced distribution in the directional domain. The number of collocation points can be so large in case of a steep solution localized in a specific region. While resolving the steep solution, one will over-resolve the smoother part of the solution, wasting the computational resources. Alternatively, we can define a mapping to cluster the Fourier-collocation points around a specified region (local refinement). This clustering can be achieved by employing a mapping for a specified region.

The *atan mapping* (Boyd, 1987, 2001) can be defined in $[-\pi,\pi]$ for the spectral direction

$$\theta = g(\chi,L) = 2\arctan[L\tan(0.5\chi)] + \chi_0, \tag{B.5}$$

where χ denotes computational space which permits the standard Fourier-collocation method for differentiation, and the constant parameter L controls the amount of clustering around the peak center χ_0. Using a change of derivative coordinate transformation for the mapping relation in Eq. (B.5), we obtain a new differentiation matrix and compute the spectral direction derivatives with them (Yildirim and Karniadakis, 2012; Yildirim, 2012).

We have found that this mapping can save us up to eight times in the number of collocation points in the directional domain. The derivation of new differentiation matrix and the demonstration of computational savings for a narrow directional spectrum was discussed in our previous work (Yildirim and Karniadakis, 2012; Yildirim, 2012).

B.3. Absorbing boundary treatment in frequency direction

The true boundary conditions for a truncated domain permit incoming waves without any reflection back to the computational domain. For the frequency direction, we have used the Absorbing Boundary Layer (ABL) approach (If et al., 1987) to satisfy non-reflective boundary conditions; this effectively *enforces periodicity* at the truncated domain boundaries.

To impose the ABL approach, we add the term $g(\sigma)\ N(\theta;x,y,t)$ to the original equation Eq. (1), and hence the new modified action balance equation is

$$\frac{\partial N(\theta,\sigma;x,y,t)}{\partial t} + \frac{\partial c_{g_x} N(\theta,\sigma;x,y,t)}{\partial x} + \frac{\partial c_{g_y} N(\theta,\sigma;x,y,t)}{\partial y} + \frac{\partial c_\theta N(\theta,\sigma;x,y,t)}{\partial \theta} + \frac{\partial c_\sigma N(\theta,\sigma;x,y,t)}{\partial \sigma} + \underbrace{g(\sigma) * N(\theta,\sigma;x,y,t)}_{\text{modificationterm}} = \frac{S(\sigma,\theta;x,y,t)}{\sigma}, \tag{B.6}$$

where $\mathbf{g}(\sigma)$ is the absorbing function, achieving zero values inside the domain and non-zero values in the absorbing layers, damping the numerical solution in these regions. The absorbing function can be defined in the computational domain ζ in $[-\pi,\pi]$ as follows:

$$g(\zeta)=\gamma_L(1-\tanh[\alpha_L(\zeta+\pi)])+\gamma_R(1+\tanh[\alpha_R(\zeta-\pi)]), \quad \text{(B.7)}$$

where γ controls the magnitude of the absorbing functions, α determines the effective width of the absorbing layers, and L and R denote the left and right layers. The parameter couples α_L and α_R control the ABL widths. We refer the interested readers for the details of the parameters to our previous work (Yildirim and Karniadakis, 2012; Yildirim, 2012).

Using the collocation differentiation Eqs. (B.2) and (B.3) in the flux form of action Eq. (B.1) with the above modification term, we can define the term $\mathcal{L}$ as

$$\mathcal{L}(\theta_k,\zeta_l,x,y,t)=\left.\frac{\partial G}{\partial\theta}\right|_{\theta=\theta_k}+J_{\zeta\sigma}\left.\frac{\partial H}{\partial\zeta}\right|_{\zeta=\zeta_l}+g(\sigma_l)N(\theta_k,\sigma_l,x,y,t)-S(\theta_l,\sigma_k,x,y,t). \quad \text{(B.8)}$$

With the above definition, the flux form equation is written as

$$\frac{\partial N}{\partial t}+\frac{\partial E}{\partial x}+\frac{\partial F}{\partial y}+\mathcal{L}(\theta_k,\zeta_l,x,y,t)=0, \quad \text{(B.9)}$$

B.4. Spatial discretizations

We will use discontinuous Galerkin (DG) (Hesthaven and Warburton, 2007; Hesthaven et al., 2007; Karniadakis and Sherwin, 1999) spectral element discretization for the geographical space. The discontinuous Galerkin formulation can be stated as: *Find an approximate solution N_h in the piece-wise polynomial space $V_h(\Omega)$, defined as $\left(V_h(\Omega)\in P^k(\Omega)\right)$ where $P^k(\Omega)$ denotes the collection of polynomials of degree up to k in the element Ω such that*

$$\int_\Omega\frac{\partial N_h}{\partial t}v_h d\Omega+\int_\Omega\frac{\partial E_h}{\partial x}v_h d\Omega+\int_\Omega\frac{\partial F_h}{\partial y}v_h d\Omega+\int_\Omega\mathcal{L}(\theta_k,\zeta_l,x,y,t)v_h d\Omega=0,\quad \forall v_h\in V_h, \quad \text{(B.10)}$$

where Ω is an arbitrary triangle element, and $\mathcal{L}$ in Eq. (B.8) is sum of spectral space derivatives, the modification term, and physical source terms which is defined above. Applying integration by parts, we obtain

$$\int_\Omega\frac{\partial N_h}{\partial t}v_h d\Omega-\int_\Omega E_h\frac{\partial v_h}{\partial x}d\Omega-\int_\Omega F_h\frac{\partial v_h}{\partial y}d\Omega+\int_{\partial\Omega}E_h v_h\cdot n dS+\int_{\partial\Omega}F_h v_h\cdot n dS+\int_\Omega\mathcal{L}(\theta_k,\zeta_l,x,y,t)v_h d\Omega=0. \quad \text{(B.11)}$$

To compute the above integrals on the standard triangle, we transform an arbitrary triangle domain Ω to a standard triangle $(-1\leqslant\xi_1+\xi_2\leqslant 1)$. To define orthogonal coordinates, we introduce a collapsed coordinate transformation that allows us to construct two-dimensional expansion functions for a triangle region the same as in a structured region. The collapsed transformation is defined as Karniadakis and Sherwin (1999)

$$\eta_1=\frac{2(1+\xi_1)}{1-\xi_2}-1;\quad \eta_2=\xi_2, \quad \text{(B.12)}$$

where η_1 and η_2 are new coordinates $-1\leqslant\eta_1,\eta_2\leqslant 1$, see Fig. B.13, removing coordinate dependency of bounds in a triangle domain $(-1\leqslant\xi_1+\xi_2\leqslant 1)$ – see Yildirim and Karniadakis (2012) and Yildirim (2012) for the details of the transformation and the final form of the equation.

Seeking approximate solution N_h expanded by orthogonal expansional functions and choosing test function v_h as the same orthogonal expansion functions (Galerkin projection) such as

$$N_h=\sum_{p=0}^{P_1}\sum_{q=0}^{P_2}u_{pq}(t)\psi_p(\eta_1)\psi_{pq}(\eta_2)\quad\text{and} \quad \text{(B.13a)}$$

$$v_h=\psi_m(\eta_1)\psi_{mn}(\eta_2), \quad \text{(B.13b)}$$

the complete polynomial space for a triangular region can be constructed $\{(pq)|0\leqslant p,q;p\leqslant P1;p+q\leqslant P_2;P_1\leqslant P_2\}$. The orthogonal expansion functions in terms of Jacobi polynomials are defined in Karniadakis and Sherwin (1999):

$$\psi_p(\eta_1)=P_p^{0,0}(\eta_1);\quad \psi_m(\eta_1)=P_m^{0,0}(\eta_1),$$
$$\psi_{pq}(\eta_2)=\left(\frac{1-\eta_2}{2}\right)^p P_q^{2p+1,0}(\eta_2);\quad \psi_{mn}(\eta_2)=\left(\frac{1-\eta_2}{2}\right)^m P_n^{2m+1,0}(\eta_2). \quad \text{(B.14)}$$

Inserting the approximate solution N_h $(N_h\in V_h)$ and test function v_h into the transformed form of Eq. (B.11) – now casted in transformed coordinates η_1 and η_2 – using Jacobi polynomials ψ_p and ψ_{pq} defined in Eq. (B.14), we will obtain the final approximated equation (see Yildirim and Karniadakis, 2012; Yildirim, 2012). We choice the upwind flux (see the other numerical flux options from Toro (1999)) to replace the boundary flux terms in Eq. (B.11).

B.5. Numerical integration of spatial and spectral terms

The discretized equations will be now reduced to an ordinary differential equation (ODE) for the expansion coefficients u_{pq}

$$\mathbf{M}_{pq,pq}\frac{du_{pq}(t)}{dt}=\frac{1}{J_{x^\xi}}\left(\mathbf{S}_{pq}+\mathbf{T}_{pq}-\mathbf{E}_{pq}-\mathbf{F}_{pq}-\mathbf{L}_{pq}\right), \quad \text{(B.15)}$$

where the mass matrix $\mathbf{M}$, the stiffness vectors $\mathbf{S}$ and $\mathbf{T}$, the edge fluxes $\mathbf{E}$ and $\mathbf{F}$, and numerical source term $\mathbf{L}$ are, respectively, the result of integrated terms in the approximate final equation. Note that the approximate equation is derived after applying the two transformations, and replacing N with N_h and v with v_h in Eq. (B.11) (see Yildirim and Karniadakis, 2012; Yildirim, 2012 for the details).

The mass matrix $\mathbf{M}$ is the result of the following quadrature integration of the time term by using the orthogonality of Jacobi polynomials $\left(\int P_m(x)P_n(x)dx=0,\quad m\neq n\right)$:

$$\mathbf{M}_{pq,pq}=\frac{2}{(1+2p)(1+p+q)}. \quad \text{(B.16)}$$

The one great advantage of using orthogonal polynomials is that the inversion of mass matrix is trivial since it is diagonal. The remaining integration terms ($\mathbf{S},\mathbf{T},\mathbf{E}$, and $\mathbf{F},\mathbf{L}$) need to be numerically computed. The details can be found in our previous work (Yildirim and Karniadakis, 2012; Yildirim, 2012). In summary, we use mixed Gauss–Lobatto/Gauss–Radau quadrature to compute each integration term.

B.6. Numerical time discretization

With regards to temporal discretization, we employed second- and third-order (Gottlieb and Shu, 1998), as well as the fourth-order explicit (5-stages) (Spiteri and Steven, 2001) *Strong Stability Preserving Runge–Kutta* (SSP-RK) schemes. The 2nd order SSP-RK schemes used in the entire study Gottlieb and Shu (1998) and Hesthaven and Warburton (2007)

$$v^{(1)}=u^n+\triangle t\ r(u^n,t^n),$$
$$u^{n+1}=\frac{1}{2}\left(u^n+v^{(1)}+\triangle t\ r(v^{(1)},t^n+\triangle t)\right), \quad \text{(B.17)}$$

where r is the right-hand side of Eq. (B.15), and $\triangle t$ is the time step size.

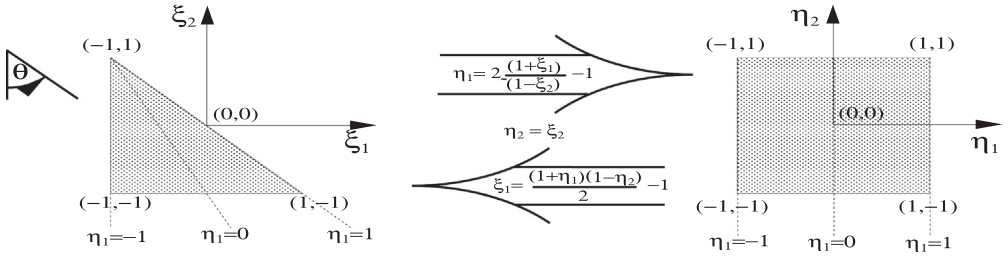

Fig. B.13. Transformation from the standard triangle to rectangular region from Karniadakis and Sherwin (1999).

Our new scheme has three distinguished features: (1) implemented on unstructured grid on physical space, (2) high accuracy (exponential convergence) in all physical spaces (geophysical space and spectral spaces), and (3) high-accuracy (2nd, 3rd, and 4th orders) in time integration schemes. The main distinction from other methods (finite element, finite volume, finite differences) (Booij et al., 1999; Hsu et al., 2005; Qi et al., 2009; Zijlema, 2010) is to have exponential convergence rather than algebraic convergence of low order methods. As an example, for a two-digit increase in solution accuracy you need to increase mesh resolution roughly 100 times for the first order scheme. On a fixed mesh spectral element codes need only to double its polynomial order. The computational cost of doubling polynomial order will be only 4 times more. The computation time increase for the first order scheme, as roughly 100 times more in this case, scales at the best linearly with the size of mesh.

The comparison of our numerical scheme and other low-order methods: (1) SWAN first order and third order schemes (Booij et al., 1999), (2) FE-WAVE's finite element scheme (Hsu et al., 2005), and (3) FVCOM-SWAVE's finite volume scheme (Qi et al., 2009) for numerical diffusion in deep water test case, introduced in Booij et al. (1999), were presented in our previous work (Yildirim and Karniadakis, 2012). The results showed that the high-order scheme using Jacobi polynomials of 2rd, 4th, 6th and 8th orders and a very coarse triangular mesh introduces minimal diffusion for the numerical diffusion test case. The result from the high-order scheme applied on this test case was most closely agreed with that of SWAN's third order scheme.

The one important issue is the so-called Garden Sprinkler effect (GSE) (Booij and Holthuijsen, 1987; Tolman, 2002; Janssen, 2008) since it is particularly pronounced for spectral discretization due to high accuracy of the scheme with minimal dissipation. The detailed discussion of GSE and the remedy for the high-order methods were proposed in our previous work (Yildirim and Karniadakis, 2012). Summarizing this discussion, we proposed to introduce selectively artificial dissipation to control GSE. The review of these efforts for the spectral methods can be found in Karniadakis and Sherwin (2005). In particular, one effective approach proposed in Yildirim and Karniadakis (2012) is the use of spectral vanishing viscosity (Tadmor, 1989), which is applied to geophysics problems in Andreassen et al. (1994) and to turbulence simulations in Karamanos and Karniadakis (2000). In our present scheme, GSE is implicitly controlled by the upwind flux in the DG formulation, an approach that suggested by Janssen in Janssen (2008).

Appendix C. Stochastic collocation, Smolyak grid, and Karhunen–Loeve (K–L) decomposition

This study uses stochastic collocation method in conjunction with Smolyak quadrature and Karhunen–Loeve decomposition to perform uncertainty quantification. We first explain the stochastic collocation method, then show that the Smolyak quadrature enables stochastic simulations for realistic computations with multiple random parameters, and finally we discuss Karhunen–Loeve decomposition to represent random processes.

C.1. Stochastic collocation

Collocation projection is applied to the stochastic differential equations constructed by expanding the random parameters in terms of orthogonal polynomials. The residual of equation is projected on collocation points, and the method assumes the residual to be zero at the collocation points. Stochastic collocation methods choose the quadrature points that are zeros of the orthogonal polynomials used in representing the stochastic solution.

Let us assume that we have the simplest form of action balance equation as function of time only:

$$\frac{dN(t)}{dt} = -S(\alpha), \tag{C.1}$$

where α represent some parameter in the source term S. Introducing the random inputs to the source term for the parameter α, the stochastic ordinary differential equation (ODE) reads:

$$\frac{d\hat{N}(t,Z)}{dt} = -S(Z), \tag{C.2}$$

where Z represents the random variable input of α. Stochastic collocation method projects the residual of the above stochastic ODE on the collocation points in the "parametric" space Z_i, which is a single value of the parameter α chosen from the known probability of random input distributions. The stochastic solution $\hat{N}(t,Z)$ can be expanded in terms of gPC polynomials (Φ_i) as

$$\hat{N}(t,Z) = \sum_{i=0}^{K} N(t)\Phi_i(Z), \tag{C.3}$$

where $N(t)$ is a deterministic solution. This expansion is inserted into Eq. (C.2) to get the residual of the equation:

$$R(t,Z) = \frac{d}{dt}\left(\sum_{i=0}^{K} N(t)\Phi_i(Z)\right) + S(Z). \tag{C.4}$$

Taking the inner product between the residual and direct delta function $\delta(Z - Z_n)$, we obtain the residual on the collocation points such as

$$(\delta(Z-Z_n), R(t,Z)) = \frac{d}{dt}\sum_{i=0} KN(t) \int \delta(Z-Z_n)S(Z)dZ + \int \delta(Z - Z_n)S(Z)dZ, \tag{C.5}$$

Since stochastic collocation methods assume that this inner product is zero, by using the Dirac delta function properties $\int \delta(x-\xi)\phi(\xi)d\xi = \phi(x)$, Eq. (C.5) becomes

$$0 = \frac{d}{dt}\left(\sum_{i=0}^{K} N(t)\ \Phi_i(Z_n)\right) + S(Z_n). \tag{C.6}$$

Recognizing the gPC expansion of $N(t,Z_n)$ as $\sum_{i=0}^{K} N(t)\ \Phi_i(Z_n)$, we get the final collocation equation as

$$\frac{dN(t,Z_n)}{dt} = -S(Z_n), \tag{C.7}$$

where Z_n is a specific value of the parameter α for the known random input. This specific value Eq. (C.7) is a deterministic ODE as is in Eq. (C.1). This is the essence of stochastic collocation methods, that is, we only need deterministic equations to solve at a specified set of collocation points (Z_n) chosen carefully in the random space.

We need to interpolate the solution from the set of deterministic solutions computed at the collocation points. The collocation points can be any set of distinct points. We have not so far constrained the set of collocation points (Z_n). But all points are equally important and some are better than others for the accuracy. To see this, let us expand a variable $S(Z)$ in terms of the gPC basis

$$\hat{N}(t,Z) = \sum_{k=0}^{K} \hat{n}_k(t)\ \Phi_k(Z), \tag{C.8}$$

where K is the order of expansion and $\hat{n}_k(t)$ are the expansion coefficients. Since we have the deterministic solutions $(N(t,Z_j))$ at points Z_j and interpolation condition $\hat{N}(t,Z_j) = N(t,Z_j)$, we can use linear system

$$\mathbf{A}^T\hat{\mathbf{n}} = \mathbf{u} \tag{C.9}$$

to solve the vector of the expansion coefficients $\mathbf{n} = (\hat{n}_0, \hat{n}_1, \ldots, \hat{n}_N)$ from M collocation points. The matrix $\mathbf{A}$

$$\mathbf{A} = \left(\Phi_i(Z_j)\right)_{K\times M}, \quad 0 \leqslant i \leqslant K, \quad 1 \leqslant j \leqslant M \tag{C.10}$$

is $K \times M$ matrix. This interpolation results in high accuracy if the set of collocation points Z_j are the zeros of the gPC orthogonal polynomials $(\Phi_i(Z))$ (quadrature points). Stochastic collocation simulation follows five basic steps: (1) provide the probability distribution of random inputs, (2) choose quadrature points for the random variable (Z_j) based on the gPC polynomials (the zeros of Jacobi, Hermite, etc. polynomials), (3) run deterministic simulations for each random parameter Z_j, (4) obtain the expansion coefficients from the linear system (C.9) to construct the stochastic solution, and (5) post-process the stochastic solution to get important statistical parameters (mean, standard deviation, etc.).

C.2. Smolyak sparse grid

The stochastic collocation points can be generated by using the tensor product of one-dimensional gPC for multi dimensional problems. From this construction, for dimensions (d) (the number of mutually independent random inputs) and the number of the collocation points (m) the total deterministic runs will be m^d. The total deterministic runs (m^d) become quickly too large for even moderate size dimensional problems. One popular approach to construct the collocation points is known as sparse grid collocation methods (Smolyak, 1963; Garcke, 2007; Xiu, 2010). The Smolyak sparse grid method is a smart way to select quadrature points from the subset of the tensor grids. An example Smolyak sparse grid superimposed on the full tensor grid is given in Fig. C.14. We refer the interested readers for the details of derivation and different applications to the work of Bungartz et al. (2004). The codes generating sparse grid are available for many numerical library and packages.

Table C.3 presents the total number of collocation points from the Smolyak Grid and tensor grids for various dimensions (N) and the orders (k). The total quadrature points from tensor product construction (m^d) for two-dimensions $(d = 2)$ is indeed lower than those of Smolyak grid. Smolyak grid does not have great advantage over the tensor production up to dimensional of five. The total

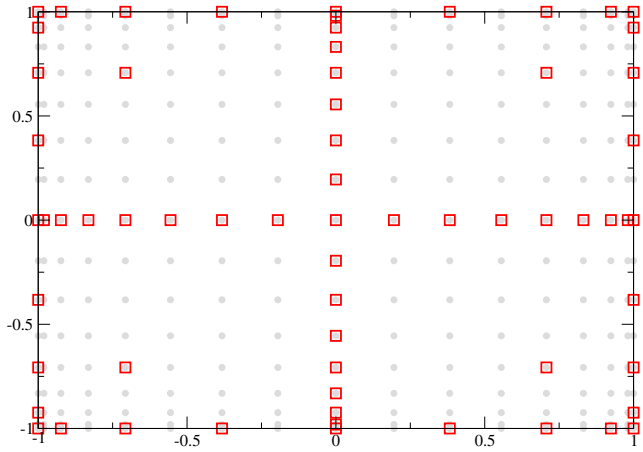

Fig. C.14. Quadrature nodes for two-dimensional $(d = 2)$ random space. Red square boxes (left) are the Clenshaw–Curtis quadrature (the extrema of Chebyshev polynomials) for $k = 4$. Total number of points is 65. The gray circles (left) represents full tensor grid. The Smolyak sparse grid is the subset of full tensor grid. (For interpretation of the references to colour in this figure legend, the reader is referred to the web version of this article.)

Table C.3
Comparison of the total number of quadrature points for various dimensions $(N = 2, 4, 8, 12, 50)$ and orders $(k = 1, 2, 3, 4)$. The right two columns present the total quadrature nodes of Smolyak sparse grid and tensor product construction.

Dimension (N)	Order(k)	Sparse grid	Tensor grid
2	1	5	4
	2	13	9
	3	29	16
	4	65	25
4	1	9	16
	2	41	81
	3	137	256
	4	401	625
8	1	17	256
	2	145	6,561
	3	849	65,536
12	1	25	4,096
	2	313	531,441
	3	2,649	16,777,216
50	1	101	$\approx 1.1 \times 10^{15}$
	2	5,101	$\approx 7.2 \times 10^{23}$
	3	171,901	$\approx 1.3 \times 10^{30}$

number of nodes on the tensor grid $((k+1)^N)$ quickly becomes a very large number for the higher dimensions as seen in Table C.3. Instead using a Smolyak grid, significant computational savings can be obtained for the higher dimensions (see Table C.3).

C.3. Karhunen–Loeve(K–L) decomposition

In the previous section, Table C.3 presented the number of quadrature points in Smolyak grid for various dimensions and orders. The number of nodes from Smolyak grid is moderate for the lower orders of higher dimensions, and that many runs of deterministic simulation is feasible on high performance computers. The total number of nodes from the Smolyak grid increases strongly for the higher dimensions $(d > 20)$, especially for high orders $(k > 3)$. For very high-dimensional problems $(d > 50)$, the total number of nodes from the Smolyak grid can also be very large.

The source parametrization which has only a few free parameters does not result in high dimensionality $(d > 20)$ in random space. On the computational mesh, random processes – which is

a function of space – such as current and boundary conditions will have very high degrees of freedom. To expedite the stochastic simulation for the random processes we can consider the relevant random process on each grid point as a random variable. It is a viable option, but this increases the dimensionality to very high values. As a specific example, to model the current field in HISWA experiment on our computational mesh in Fig. 2(b) we might require about 500 random variables; each represents random variable for the current at the collocation points on the computational mesh. Low-order methods (finite volume, finite element) will even have much higher degrees of freedom for the same problem.

To parametrize random processes due to very high dimensionality, some dimensionality reduction techniques are necessary. Karhunen–Loeve (KL) (Loeve, 1977) is one of the most popular approach with regards to this issue. The mathematical representation and derivation can be found in Section 5.3.

References

Abdalla, S., Cavaleri, L., 2002. Effect of wind variability and variable air density on wave modelling. J. Geophys. Res. 107 (C7), 17.

Andreassen, Øyvind, Lie, I., Wasberg, C.E., 1994. The spectral viscosity method applied to simulation of waves in a stratified atmosphere. J. Comput. Phys. 110 (2), 257–273.

Battjes, J.A., 1994. Shallow water wave modeling. In: Isaacson, M., Quick, M. (Eds.), Proc. Int. Symp.: Waves – Physical and Numerical Modelling, Univ. of British Columbia. ASCE, Vancouver, pp. 1–23.

Battjes, J.A., Janssen, J.P.F.M., 1978. Energy loss and set-up due to breaking of random waves. In: Proceedings of the 16th International Conference on Coastal Engineering. ASCE, pp. 569–587.

Battjes, J.A., Stive, M.J.F., 1985. Calibration and verification of a dissipation model for random breaking waves. J. Geophys. Res. 90 (C5), 9159–9167.

Benoit, M., 2005. Evaluation of methods to compute the non-linear quadruplet interactions for deep-water wave spectra. In: Proc. 5th Int. Symp. on Ocean Waves, Measurement and Analysis, WAVES 2005. ASCE.

Bonekamp, H., Komen, G.J., Sterl, A., 2002. Statistical comparisons of observed and ECMWF modeled open ocean surface drag. J. Phys. Oceanogr. 32, 1010–1027.

Booij, N., Holthuijsen, L.H., 1987. Propagation of ocean waves in discrete spectral wave models. J. Comput. Phys. 68, 307–326.

Booij, N., Ris, R.C., Holthuijsen, L.H., 1999. A third-generation wave model for coastal regions. J. Geophys. Res. 104, 7649–7666.

Bouws, E., Battjes, J.A., 1982. A monte Carlo approach to the computation of refraction of water waves. J. Geophys. Res. 87 (C8), 15.

Bouws, E., Komen, G.J., 1983. On the balance between growth and dissipation in an extreme depth-limited wind-sea in the southern North Sea. J. Phys. Oceanogr. 13, 1653–1658.

Bouws, E., Komen, G.J., 1983. On the balance between growth and dissipation in an extreme depth-limited wind-sea in the southern North Sea. J. Phys. Oceanogr. 13, 1653–1658.

Boyd, J.P., 1987. Orthogonal rational functions on a semi-infinite interval. J. Comput. Phys. 70 (1), 63–88.

Boyd, J.P., 1988. Chebyshev domain truncation is inferior to Fourier domain truncation for solving problems on an infinite interval. J. Sci. Comput. 3 (2), 109–120.

Boyd, J.P., 2001. Chebyshev and Fourier Spectral Methods: Second Revised Edition, second ed. Dover Publications.

Breugem, W.A., Holthuijsen, L.H., 2007. Generalized shallow water wave growth from lake George. J. Waterway, Port, Coastal, Ocean Eng. 133 (3), 173–182.

Buizza, R., Palmer, T.N., 1995. The singular-vector structure of the atmospheric global circulation. J. Atmos. Sci. 52 (9), 1434–1456.

Bungartz, H.-J., Griebel, M., 2004. Sparse grids. Acta Numer. 13, 147–269.

Cavaleri, L., Alves, J.-H.G.M., Ardhuin, F., Babanin, A., Banner, M., Belibassakis, K., Benoit, M., Donelan, M., Groeneweg, J., Herbers, T.H.C., Hwang, P., Janssen, P.A.E.M., Janssen, T., Lavrenov, I.V., Magne, R., Monbaliu, J., Onorato, M., Polnikov, V., Resio, D., Rogers, W.E., Sheremet, A., Smith, J.M., Tolman, H.L., van Vledder, G., Wolf, J., Young, I., 2007. Wave modelling – the state of the art. Prog. Oceanogr. 75 (4), 603–674.

Charnock, H., 1955. Wind stress on a water surface. Q. J. R. Meteorol. Soc. 81, 639.

Clenshaw, C.W., Curtis, A.R., 1960. A method of numerical integration on an automatic computer. Numer. Math. 2, 197–205.

Cockburn, B., Karniadakis, G.E., Shu, C.W., 2000. Discontinuous Galerkin Methods. Springer.

Dingemans, M.W., 1987. Verification of numerical wave propagation models with laboratory measurements: Hiswa verification in the directional wave basin. Tech. rep., Delft Hydraulics.

Dingemans, M.W., Stive, M.J.F., Bosma, J., deVriend, H.J., Vogel, J.A., 1986. Directional nearshore wave propagation and induced currents. In: Proceedings of the 20th Conference on Coastal Engineering. ASCE, pp. 1092–1106.

Ehrendorfer, M., Tribbia, J.J., 1997. Optimal prediction of forecast error covariances through singular vectors. J. Atmos. Sci. 54, 286–313.

Eldeberky, Y., 1996. Nonlinear Transformation of Wave Spectra in the Nearshore Zone (Ph.D. thesis). TUDelft.

Fishman, G.S., 1996. Monte Carlo: Concepts, Algorithms, and Applications. Springer-Verlag.

Garcke, J., TUBerlin, 2007. Sparse grid tutorial.

Gelaro, R., Buizza, R., Palmer, T.N., Klinker, E., 1997. Sensitivity analysis of forecast errors and the construction of optimal perturbations using singular vectors. J. Atmos. Sci. 55, 1012–1037.

Ghanem, R.G., Spanos, P., 1991. Stochastic Finite Elements: A Spectral Approach. Springer-Verlag.

Gottlieb, D., Orszag, S.A., 1977. Numerical Analysis of Spectral Methods: Theory and Applications. SIAM-CMBS, Philadelphia.

Gottlieb, S., Shu, C.-W., 1998. Total variation diminishing Runge–Kutta schemes. Math. Comput 67, 73–85.

Hartmann, D.L., Buizza, R., Palmer, T.N., 1995. Singular vectors: the effect of spatial scale on linear growth of disturbances. J. Atmos. Sci. 52, 3885–3894.

Hasselmann, K., 1962. On the non-linear energy transfer in a gravity wave spectrum, part 1: general theory. J. Fluid Mech. 12, 481–501.

Hasselmann, K., 1963a. On the non-linear energy transfer in a gravity wave spectrum Part 2: conservation theorems; wave-particle analogy; irreversibility. J. Fluid Mech. 15, 273–282.

Hasselmann, K., 1963b. Part 3. evaluation on the energy flux and swell-sea interaction for a Neumann spectrum. J. Fluid Mech. 15, 467–483.

Hasselmann, K., Barnett, T.P., Bouws, E., Carlson, H., Cartwright, D.E., Enke, K., Ewing, J.A., Gienapp, H., Hasselmann, D.E., Kruseman, P., Meerburg, A., Müller, P., Olbers, D.J., Richter, K., Sell, W., Walden, H., 1973. Measurements of wind-wave growth and swell decay during the joint North Sea wave project. Deut. Hydrogr. Z. 8 (12), 1–95, suppl. A..

Hasselmann, K., Collins, J.I., 1968. Spectral dissipation of finite depth gravity waves due to turbulent bottom friction. J. Mar. Res. 26, 1–12.

Hasselmann, S., Hasselmann, K., 1985. Computation and parametrization of the nonlinear energy transfer in a gravity-wave spectrum. part I: a new method for efficient computations of the exact nonlinear transfer. J. Phys. Oceanogr. 15, 1369–1377.

Hesthaven, J.S., Gottlieb, S., Gottlieb, D., 2007. Spectral Methods for Time-Dependent Problems. Cambridge University Press.

Hesthaven, J.S., Warburton, T., 2007. Nodal Discontinuous Galerkin Methods: Algorithms, Analysis, and Applications. Springer Publishing Company, Incorporated.

Holthuijsen, L.H., 2007. Waves in Oceanic and Coastal Waters. Cambridge University Press.

Holthuijsen, L.H., Booij, N., Herbers, T.H.C., 1989. A prediction model for stationary, short-crested waves in shallow water with ambient currents. Coast. Eng. 13, 23–54.

Hsu, T.-W., Ou, S.-H., Liau, J.-M., 2005. Hindcasting nearshore wind waves using a fem code for swan. Coast. Eng. 52, 177–195.

If, F., Berg, P., Christiansen, P.L., Skovgaard, O., 1987. Split-step spectral method for nonlinear Schrödinger equation with absorbing boundaries. J. Comput. Phys. 72 (2), 501–503.

Janssen, P., 2004. The Interaction of Ocean Waves and Wind. Cambridge University Press.

Janssen, P.A.E.M., 2008. Progress in ocean wave forecasting. J. Comput. Phys. 227 (7), 3572–3594.

Karamanos, G.-S., Karniadakis, G.E., 2000. A spectral vanishing viscosity method for large-eddy simulations. J. Comput. Phys. 163 (1), 22–50.

Karniadakis, G.E., Sherwin, S.J., 1999. Spectral/hp Element Methods for CFD. Oxford University Press.

Karniadakis, G.E., Sherwin, S.J., 2005. Spectral/hp Element Methods for CFD,, Oxford University Press.

Komen, G.J., Cavaleri, L., Donelan, M., Hasselmann, K., Hasselmann, S., Janssen, P.A.E.M., 1994. Dynamics and Modeling of Ocean Waves. Cambridge University Press, Cambridge.

Komen, G.J., Hasselmann, K., Hasselmann, S., 1984. On the existence of a fully developed wind sea spectrum. J. Phys. Oceanogr. 14, 1271–1285.

Krasnopolsky, V.M., Chalikov, D.V., Tolman, H.L., 2002. A neural network technique to improve computational efficiency of numerical oceanic models. Ocean Model. 4 (34), 363–383.

Kuik, A.J., Vledder, G.P.V., Holthuijsen, L.H., 1988. A Method for the routine analysis of pitch-and-roll buoy wave data. J. Phys. Oceanogr. 18, 1020–1034.

Lavrenov, I.V., 2003. Optimal numerical realization of the energy balance equation for wind wave models. In: Proceedings of the 2003 International Conference on Computational Science: Part II. ICCS'03. Springer-Verlag, pp. 179–187.

Lin, R.Q., Perrie, W., 1998. On the mathematics and approximation of the nonlinear wave-wave interactions. Nonlinear Ocean Waves, Adv. Fluid Mech., 61–88.

Loeve, M., 1977. Probability Theory. Springer-Verlag.

Longuet-Higgins, M.S., Stewart, R.W., 1961. The changes in amplitude of short gravity waves on steady non-uniform currents. J. Fluid Mech. 10 (04), 529–549.

Madsen, P.A., Srenson, O., 1993. Bound waves and triad interactions in shallow water. Ocean Eng. 20, 359–388.

Morris, M.D., 1991. Factorial sampling plans for preliminary computational experiments. Technometrics 33 (2), 161–174.

Palmer, T.N., Gelaro, R., Barkmeijer, J., Buizza, R., 1997. Singular Vectors, metrics, and adaptive observations. J. Atmos. Sci. 54, 286–313.

Phillips, O.M., 1966. The Dynamics of the Upper Ocean. Cambridge University Press.

Plant, N.G., Holland, K.T., 2011. Prediction and assimilation of surf-zone processes using a Bayesian network: Part I: forward models. Coast. Eng. 58 (1), 119–130.

Plant, N.G., Holland, K.T., 2011. Prediction and assimilation of surf-zone processes using a Bayesian network: Part II: inverse models. Coast. Eng. 58 (3), 256–266.
Ponce, S., Ocampo-Torres, F.J., 1998. Sensitivity of a wave model to wind variability. J. Geophys. Res. 103 (C2), 22.
Qi, J., Chen, C., Beardsley, R.C., Perrie, W., Cowles, G.W., Lai, Z., 2009. An unstructured-grid finite-volume surface wave model (fvcom-swave): implementation, validations and applications. Ocean Model. 28 (1–3), 153–166.
Ris, R.C., 1997. Spectral Modeling of Wind Waves in Coastal Areas (Ph.D. thesis). TUDelft.
Roulston, M.S., Ellepola, J., Hardenberg, J.V., Smith, L.A., 2005. Forecasting wave height probabilities with numerical weather prediction models. Ocean Eng. 32 (14–15), 1841–1863.
Saltelli, A., Ratto, M., Andres, T., Campolongo, F., Cariboni, J., Gatelli, M.S., Tarantola, S., 2008. Global Sensitivity Analysis. John Wiley & Sons.
Smolyak, S.A., 1963. Quadrature and interpolation formulas for tensor products of certain classes of functions. Sov. Math. Dokl. 4, 240–243.
Snyder, R.L., Thacker, W.C., Hasselmann, K., Hasselmann, S., Barzel, G., 1993. Implementation of an efficient scheme for calculating nonlinear transfer from wave–wave interactions. J. Geophys. Res.: Oceans 98 (C8), 14507–14525.
Spiteri, R.J., Steven, Ruuth J., 2001. A new class of optimal high-order strong-stability-preserving time discretization methods. SIAM J. Numer. Anal 40, 469–491.
SWAMP Group, 1985. Ocean wave modeling. Plenum Press, New York.
Tadmor, E., 1989. Convergence of spectral methods for nonlinear conservation laws. SIAM J. Numer. Anal. 26, 30–44.
Thacker, W.C., Srinivasan, A., Iskandarani, M., Knio, O.M., Hnaff, M.L., 2012. Propagating boundary uncertainties using polynomial expansions. Ocean Model. 43, 52–63.
Tolman, H. L., 1995. On the selection of propagation schemes for a spectral wind wave model. Tech. Rep., NWS/NCEP Office.
Tolman, H.L., 2002. Alleviating the garden sprinkler effect in wind wave models. Ocean Model. 4, 269–289.
Tolman, H.L., Grumbine, R.W., 2013. Holistic genetic optimization of a generalized multiple discrete interaction approximation for wind waves. Ocean Model. 70, 25–37.
Tolman, H.L., Krasnopolsky, V.M., 2006. Nonlinear interactions in practical wind wave models. Tech. Rep., JCOMM Tech. Rep.
Tolman, H.L., Krasnopolsky, V.M., Chalikov, D.V., 2005. Neural network approximations for nonlinear interactions in wind wave spectra: direct mapping for wind seas in deep water. Ocean Model. 8 (3), 253–278.
Toro, E.F., 1999. Riemann Solvers and Numerical Methods for Fluid Dynamics. Springer.
van Vledder, G.P., 2006. The wrt method for the computation of non-linear four-wave interactions in discrete spectral wave models. Coast. Eng. 53 (23), 223–242.
van Vledder, G.P., Herbers, T.H.C., Jensen, R.E., Resio, D.T., Tracy, B., 2000. Modelling of non-linear quadruplet wave-wave interactions in operational wave models. In: Proceedings of the 27th International Conference on Coastal Engineering. ASCE, Sydney, Australia, pp. 797–811.
WAMDI Group, 1988. The WAM model – a third generation ocean wave prediction model. J. Phys. Oceanogr. 18, 1775–1810.
Whitham, G.B., 1974. Linear and Nonlinear Waves. Wiley, New York.
Wood, D.J., Muttray, M., Oumeraci, H., 2001. The swan model used to study wave evolution in a flume. Ocean Eng. 28 (7), 805–823.
Xiu, D., 2010. Numerical Methods for Stochastic Computations. Princeton University Press.
Xiu, D., Hesthaven, J., 2005. High-order collocation methods for differential equations with random inputs. SIAM J. Sci. Comput. 27 (3), 1118–1139.
Xiu, D., Karniadakis, G.E., 2002. The Wiener–Askey polynomial chaos for stochastic differential equations. SIAM J. Sci. Comput. 24, 619–644.
Yildirim, B., 2012. Topics in Numerical Ocean Simulation (Ph.D. thesis). Brown University.
Yildirim, B., Karniadakis, G.E., 2012. A hybrid spectral/DG method for solving the phase-averaged ocean wave equation: algorithm and validation. J. Comput. Phys. 231 (14), 4921–4953.
Young, I.R., 1999. Wind Generated Ocean Waves. Elsevier Science, Oxford.
Young, I.R., Verhagen, L.A., 1996. The growth of fetch limited waves in water of finite depth. Part 1. Total energy and peak frequency. Coast. Eng. 29 (1–2), 47–78.
Zijlema, M., 2010. Computation of wind-wave spectra in coastal waters with swan on unstructured grids. Coast. Eng. 57 (3), 267–277.
Zijlema, M., van Vledder, G.P., Holthuijsen, L.H., 2012. Bottom friction and wind drag for wave models. Coast. Eng. 65, 19–26.